

Review

# Application of the Heptacyanidorhenate(IV) as a Metalloligand in the Design of Molecular Magnets

Kira E. Vostrikova 

Nikolaev Institute of Inorganic Chemistry SB RAS, 3 Lavrentiev Avenue, Novosibirsk 630090, Russia; vosk@niic.nsc.ru

**Abstract:** This review is devoted to an analysis of currently known heterometallic molecular magnets based on an orbitally degenerate  $5d$  metalloligand,  $[\text{Re}^{\text{IV}}(\text{CN})_7]^{3-}$ . Heptacyanidometallates with a pentagonal bipyramidal structure of the coordination site and degenerate ground spin state are the source of anisotropic magnetic exchange interactions upon the formation of cyanide-bonded assemblies involving the paramagnetic complexes of the first transition series. Therefore, the development of methods for chemical design using such molecular magnetic modules is extremely important. If for the  $4d$  congener, isoelectronic  $[\text{Mo}^{\text{III}}(\text{CN})_7]^{3-}$ , a family of approximately 40 heterometallic compounds, was obtained, whereas for heptacyanorhenate(IV), no more than 20 are known. However, as a result of recent studies, heterobimetallic magnetic assemblies of all dimensionalities have been synthesized, from 0D to 1D, demonstrating slow magnetization relaxation, to 2D networks and 3D frameworks possessing large magnetic hysteresis. The most anisotropic is a 2D network,  $\text{PPN}[\text{Mn}^{\text{III}}(\text{acacen})_2\text{Re}^{\text{IV}}(\text{CN})_7]\cdot\text{Solv}$ , with a critical temperature of 20 K and magnetic hysteresis with a record coercivity for cyanide-bridged molecular materials.

**Keywords:** heptacyanidorhenate(IV); cyanide-bridged heterometallic assemblies; manganese(III) Schiff base complexes; orbitally degenerate  $5d$  complex; pentagonal bipyramidal cyanidometallate; 1D coordination polymer; 2D coordination network; 3D coordination polymer; single-chain magnet; slow magnetic relaxation



**Citation:** Vostrikova, K.E. Application of the Heptacyanidorhenate(IV) as a Metalloligand in the Design of Molecular Magnets. *Magnetochemistry* **2022**, *8*, 189. <https://doi.org/10.3390/magnetochemistry8120189>

Academic Editors: Marius Andruh and Eva Rentschler

Received: 14 November 2022

Accepted: 7 December 2022

Published: 14 December 2022

**Publisher's Note:** MDPI stays neutral with regard to jurisdictional claims in published maps and institutional affiliations.



**Copyright:** © 2022 by the author. Licensee MDPI, Basel, Switzerland. This article is an open access article distributed under the terms and conditions of the Creative Commons Attribution (CC BY) license (<https://creativecommons.org/licenses/by/4.0/>).

## 1. Introduction

Orbitally degenerate coordination compounds of heavier  $d$ -metal ions with unquenched orbit angular momentum and a strong spin orbital interaction are promising in the design of highly anisotropic magnetic materials. It was first theoretically predicted that  $4d/5d$  heptacyanidometallates are especially efficient in introducing strong anisotropy in heterometallic molecular systems [1,2], which was confirmed experimentally by preparation of a row of single-molecule magnets (SMMs) involved in these metalloligands [3–8]. Its main property is the absence of single-ion magnetic anisotropy owing to their low-spin ground state ( $S = 1/2$ ). In this case, magnetic anisotropy is created cooperatively, together with bounded high-spin  $3d$  complexes through pair-ion anisotropic exchange interactions.

In contrast to the relatively numerous cyano-bridged unidimensional magnetic assemblies comprising  $3d$  centers [9–13], single-chain magnets (SCMs) including polycyanides of heavier  $d$  metals are less known [14–19]. Among them, chains involving low-spin ( $S = 1/2$ ), orbitally degenerate cyanidometallates are extremely rare, with only a few SCMs comprising  $\text{Fe}^{\text{III}}$  [20–23] and  $\text{Os}^{\text{III}}$  cyanides [14] and five 1D coordination polymers involving pentagonal bipyramidal (PBP)  $[\text{Mo}(\text{CN})_7]^{4-}$  ( $4d^3$ ) [8,24,25], only three of which are SCMs. The only known 2D anionic network is a compound,  $\text{K}_2\text{Mn}_3(\text{H}_2\text{O})_6[\text{Mo}(\text{CN})_7]_2\cdot 6\text{H}_2\text{O}$  [26]. In contrast, 3D heterobimetallic assemblies based on orbitally degenerate heavy  $d$  cyanidometallates are more common. Eleven bimetallic frameworks based on  $[\text{Mo}^{\text{III}}(\text{CN})_7]^{4-}$  have been obtained [8], including five 3D polymers: one neutral material, i.e.,  $\text{Mn}_2(\text{H}_2\text{O})_5\text{Mo}(\text{CN})_7\cdot 4\text{H}_2\text{O}$  [27] and four anionic complexes— $[\text{Mn}(\text{dpop})]_3[\text{Mn}(\text{dpop})\text{H}_2\text{O}][\text{Mo}(\text{CN})_7]_2\cdot 13.5\text{H}_2\text{O}$  or

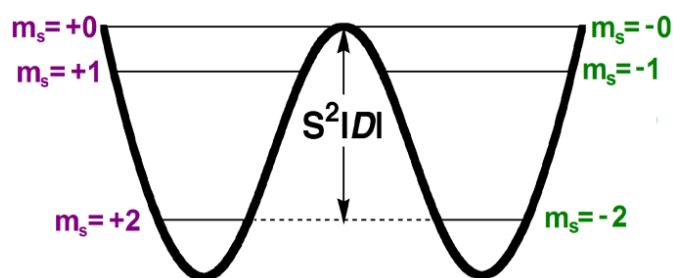
[Mn(dpop)]<sub>2</sub>[Mo(CN)<sub>7</sub>]·2H<sub>2</sub>O [7], [Mn<sub>2</sub>(pyrim)<sub>2</sub>Mo(CN)<sub>7</sub>]·2H<sub>2</sub>O, and one involving V(II) [V<sub>2</sub>(pyrim)<sub>2</sub>Mo(CN)<sub>7</sub>]·xH<sub>2</sub>O [28].

Although heptacyanidorhenate (IV) (5d<sup>3</sup>) is much more resistant to light and atmospheric oxygen than its 4d congener, its heterobimetallic compounds are less studied. Furthermore, it should be especially noted that an absence of a large amount of [Re<sup>IV</sup>(CN)<sub>7</sub>]<sup>3-</sup> assemblies with Mn<sup>II</sup> ions possessing a maximum number of unpaired electrons for a 3d ion is associated with a reduction of Re<sup>IV</sup> ions.

The aim of this report is to review all currently known heterometallic compounds involving an [Re<sup>IV</sup>(CN)<sub>7</sub>]<sup>3-</sup> anion as a source of anisotropic coupling, which is extremely important in the design of high-performance, low-dimensional nanomagnets, as the use of heavier cyanidometallates has its benefits. First and foremost, versus their 3d congeners, they have higher anisotropy and more diffuse orbitals, offering stronger magnetic exchange interactions [5].

## 2. Theoretical Background

LD magnetic systems (0D and 1D) are molecular polynuclear complexes, which have a ground state with a high spin displaying slow relaxation of magnetization, in combination with a hysteresis loop under the blocking temperature ( $T_B$ ). In SMMs, this takes place because of a bistability. The interaction between the spins is defined by a Hamiltonian,  $H = D[S_z^2 - S(S + 1)/3] + E(S_x^2 - S_y^2)$ , where  $D$  and  $E$  are the zero field-splitting (ZFS) constants [29,30]. When the axial parameter  $D$  is negative, the system potential is described by a double-well function (Scheme 1). For this reason, the two lowest quantum states,  $+M_s$  and  $-M_s$ , are separated by an anisotropy barrier ( $U_{eff}$ ) to be overcome for magnetization reversing. The constant  $E$  denotes an axial distortion. Therefore, the barrier energy dependence includes a high-spin ground state ( $S$ ) and magnetic anisotropy ( $D$ ):  $U_{eff} = |D|S^2$  and  $|D|(S^2 - 1/4)$  for integer and half-integer spins, respectively [29,30]. Note that in first-row transition metal complexes, ZFS is the most common source of magnetic anisotropy. The anisotropy constants are decisive in the processes of slow magnetic relaxation [31]. This situation relates to systems with uniaxial anisotropy (called Ising anisotropy), for which  $D$  should be large, while  $E$  should be as small as possible to prevent binding among  $m_s$  components. Such a coupling is responsible for tunneling between two energy equal states  $m_s = \pm 1$ .



**Scheme 1.** Energy barrier ( $U_{eff}$ ) for a hypothetical  $S = 2$  single-molecule magnet.

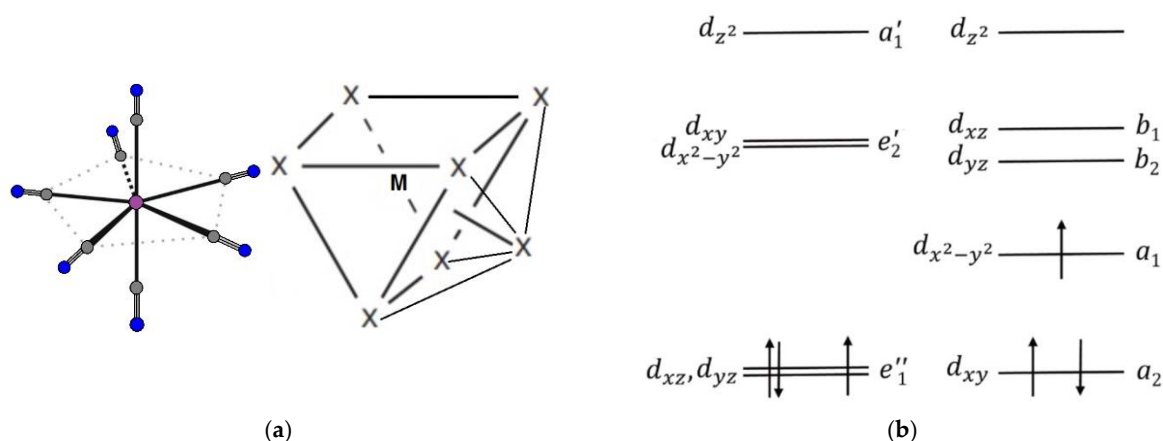
The 1D coordination polymers are also able to display slow magnetic relaxation [32]. The SCMs take precedence over SMMs to obtain higher anisotropy barriers. This profit originates from an addendum in  $U_{eff}$ ,  $\Delta_{\xi}$  named correlation energy, the source of the latter being an exchange coupling ( $J$ ) between the spins. Considering that a spin–spin coupling is  $-2JS_1 \cdot S_2$ , for an isotropic model (Ising limit),  $\Delta_{\xi} = 4|J|S^2$  when  $|D/J| > 4/3$ . In the case of  $|D| \ll |J|$  (Heisenberg limit)— $\Delta_{\xi} = 4S^2|JD|^{1/2}$  [10]. Then, the total spin–reversal barrier for an infinite magnetic wire is  $U_{eff} = \Delta_A + 2\Delta_{\xi}$  [33,34]. However, in a finite-length 1D polymer,  $U_{eff} = \Delta_A + \Delta_{\xi}$  owing to a nucleation effect of the chain ends [35].

If there are no long-range magnetic ordering at a certain temperature, the LD molecular compounds are capable to lock their magnetization after switching the field. This is due to slow magnetic relaxation going down  $T_B$ . In such a relaxation process, anisotropy plays

a key role. For the majority octahedral complexes, there is no anisotropy for a perfect  $O_h$  symmetry. For the  $3d$  complexes, a symmetry lowering through octahedron distortion is a source of magnetic anisotropy. However, it is difficult to rationally set such a deformation in complexes of  $Co^{2+}$ ,  $Mn^{3+}$ , and  $Ni^{2+}$  coordination compounds, which exhibit anisotropy with  $|D| < 10 \text{ cm}^{-1}$  [30].

Heptacyanidometallates  $[M(CN)_7]^{n-}$  ( $M = Mo^{III}$   $n = 4$  [1,8,36] or  $Re^{IV}$   $n = 3$  [3,37,38]) represent the metalloligand with almost ideal PBP polyhedrons; such a geometry pre-determines the exchange interactions with a greater degree of anisotropy with high-spin  $3d$  metal complexes. This is due to the strong spin-orbit coupling (SOC) resulting from an unquenched orbital momentum (L) of PBP heptacyanides [1,2,39].

The heptacoordinated environment of the central atom in a homoleptic complex can be realized in two ways: a pentagonal bipyramid ( $D_{5h}$ ) or a less symmetrical monocapped trigonal prism ( $C_{2v}$ ). Various coordination polyhedra of the central ion lead to various ligand field-splitting diagrams and ground states with diverse electronic configurations (Scheme 2). For a metal at the center of a pentagonal bipyramid, the  $D_{5h}$  symmetry provides a doubly degenerated  ${}^2E_1-(e_1'')$ <sup>3</sup> electronic configuration to the ground state, whereas in the case of a monocapped trigonal prism with  $C_{2v}$  symmetry, the ground configuration state is denoted as  ${}^2A_1-(a_2)^2(a_1)^1$ . From the available crystallographic data for  $[Mo^{III}(CN)_7]^{4-}$ -based assemblies [8,40], it can be concluded that for LD compounds, the PBP geometry of the coordination polyhedron is realized; for 2D and 3D compounds, on the contrary, MCP polyhedrons are quite common. For  $Re^{IV}$ , the only case of MCP geometry was observed in the 2D assembly of  $\{(Mn^{5Me}Salen)_6(H_2O)_2Re(CN)_7\}$  clusters, and will be discussed in the final part of the current review.



**Scheme 2.** (a) Pentagonal bipyramid (PBP) (left) and MCP geometry of  $[M(CN)_7]^{3-/4-}$ ; (b) ligand field energy level diagrams and ground-state electronic configurations for a PBP (left) and monocapped trigonal prism (right) of  $[M(CN)_7]^{3-/4-}$ .

### 3. Heterobimetallic Assemblies Based on Pentagonal Bipyramidal Tecton $[Re^{IV}(CN)_7]^{3-}$

#### 3.1. $[Re^{IV}(CN)_7]^{3-}$ Metalloligand

Despite the fact that n-tetrabutylammonium heptacyanidorhenate(IV) (Scheme 2a) was first obtained 20 years ago [38], relatively few heterometallic compounds have been obtained with this metalloligand. The latter was synthesized by a ligand exchange reaction:  $(n-Bu_4N)_2[ReCl_6] + 7(n-Bu_4N)CN = (n-Bu_4N)_3[Re(CN)_7]$ , **1**. The physical properties of  $[Re(CN)_7]^{3-}$  are associated with the  ${}^2E_1''$  ground state of a PBP environment and a low-spin  $d^3$  electron configuration ( $\mu_{eff} = 2.02 \mu_B$ ,  $g_{av} = 2.33$ ). EPR study confirms the anisotropy of the g factor ( $g_{||} = 3.66$  and  $g_{\perp} = 1.59$ ) displaying  $A_{||} = 129 \text{ G}$ , a hyperfine splitting in the parallel component. The lowest in energy spin allowed a component of the  $e_1'' \rightarrow e_2'$  transition of  $[Re^{IV}(CN)_7]^{3-}$ , which is responsible for a peak at  $25,300 \text{ cm}^{-1}$  (395 nm) in the

electronic absorption spectrum of **1**, whereas for  $[\text{Mo}(\text{CN})_7]^{4-}$ , a similar transition arises at  $24,900\text{ cm}^{-1}$  [40].

### 3.2. Reduction to $[\text{Re}^{\text{III}}(\text{CN})_7]^{3-}$ by $\text{M}^{\text{II}}$

Prolonged heating of an aqueous solution of **1** and  $\text{MnCl}_2$  at  $85\text{ }^\circ\text{C}$  yielded the 3D polymer compound  $[\text{fac-Mn}(\text{H}_2\text{O})_3][\text{cis-Mn}(\text{H}_2\text{O})_2][\text{Re}(\text{CN})_7]\cdot 3\text{H}_2\text{O}$  (**2**) [38], exhibiting a complicated polymorphic transform like to that found for  $[\text{mer-Mn}(\text{H}_2\text{O})_3][\text{cis-Mn}(\text{H}_2\text{O})_2][\text{Mo}(\text{CN})_7]\cdot 4\text{H}_2\text{O}$  [27]. The use of noncoordinating oxidants to prevent rhenium reduction resulted in  $[\text{Re}^{\text{V}}(\text{CN})_8]^{3-}$  formation.

The interaction of **1** with  $[(\text{Py}_5\text{Me}_2)\text{Mn}^{\text{II}}(\text{MeCN})](\text{PF}_6)_2$  (**3**) ( $S = 5/2$ ) in acetonitrile solution leads to a blue compound  $[(\text{Py}_5\text{Me}_2)_4\text{Mn}_4\text{Re}(\text{CN})_7](\text{PF}_6)_5\cdot 6\text{H}_2\text{O}$  (**4**) [3]. Under ambient conditions, the reaction mixture color changes from blue to green, then to yellow, forming the once-reduced complex  $[(\text{Py}_5\text{Me}_2)_4\text{Mn}_4\text{Re}(\text{CN})_7](\text{PF}_6)_4\cdot 10\text{H}_2\text{O}$  (**5**). Crystal structures show that the both molecules have a cross-like form, wherein four  $[(\text{Py}_5\text{Me}_2)\text{Mn}]^{2+}$  elements are attached to a central PBP  $[\text{Re}(\text{CN})_7]^{3-/4-}$  anion (Figure 1).

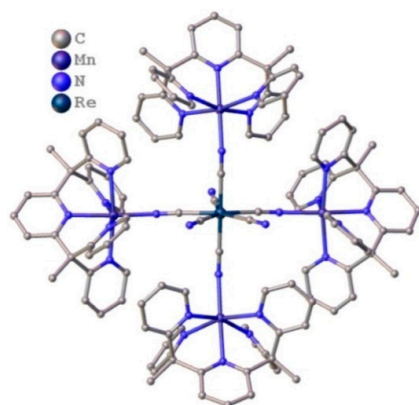


**Figure 1.** Cross-like geometry of the pentanuclear cations of  $[(\text{Py}_5\text{Me}_2)_4\text{Mn}_4\text{Re}(\text{CN})_7](\text{PF}_6)_5\cdot 6\text{H}_2\text{O}$  (**4**) and  $[(\text{Py}_5\text{Me}_2)_4\text{Mn}_4\text{Re}(\text{CN})_7](\text{PF}_6)_4\cdot 10\text{H}_2\text{O}$  (**5**). Hydrogens atoms are omitted for clarity.

Treatment of the *dc* (Figure 2a) and *ac* (Figure 3) data of **4** revealed ferromagnetic spin coupling between the metal ions, an  $S = 21/2$  ground state, with axial ZFS of  $D = -0.44\text{ cm}^{-1}$ , as the SMM parameters of **4**:  $U_{\text{eff}} = 33\text{ cm}^{-1}$  and  $\tau_0 = 2.4 \times 10^{-8}\text{ s}$ . Under ambient conditions, a one-electron reduction of Re ions occurred in **4**, affording the paramagnetic complex **5** with four noninteracting  $\text{Mn}^{\text{II}}$  centers [3].

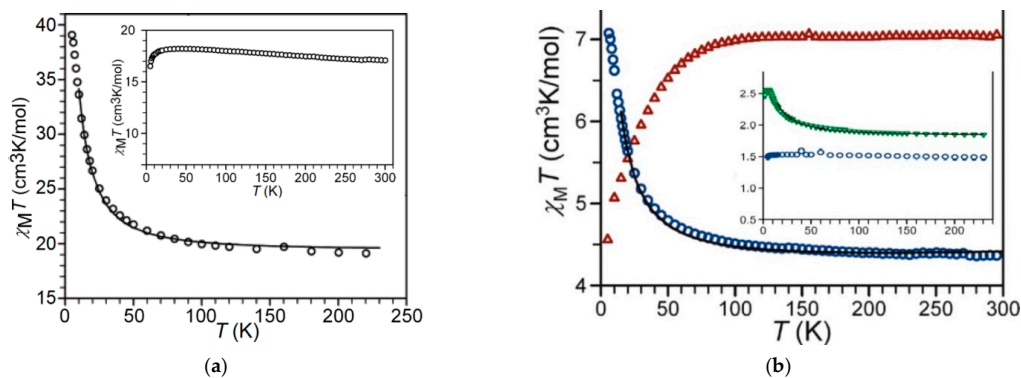


**Figure 2.** Variable temperature of the *dc* magnetic susceptibility data obtained in a field of 1000 Oe in the range of 2–300 K: (a) for **4** and **5** (inset); the solid line is a simulation plot with  $J = +2.3\text{ cm}^{-1}$  and  $g = 2.00$  [3]. (b) **6** (red) and **7** (blue). Inset:  $\chi T$  plots for  $\text{Cu}_4\text{Re}$  species **8** (green) and **9** (blue); the black plots are a simulation resulting in  $J = +4.4$  and  $+6.26\text{ cm}^{-1}$  for **7** and **8**, respectively [4].

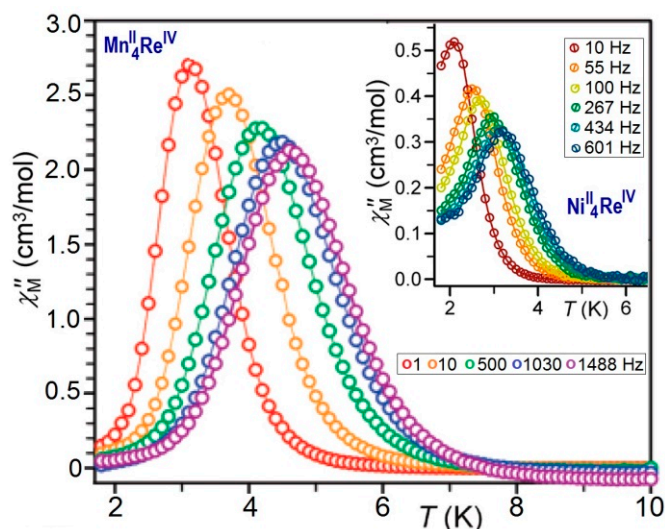


**Figure 3.** Variable-temperature imaginary parts of ac magnetic susceptibility data for **4** and **9** (inset) obtained in a 4 Oe oscillating field at different frequencies [3,4].

The reaction between the heptacyanidorhenate(IV) and  $[(\text{Py}_5\text{Me}_2)\text{M}(\text{MeCN})]^{2+}$  ( $\text{M} = \text{Co}, \text{Ni}, \text{Cu}$ ) yields a number of pentanuclear complex cations of the general formula  $[(\text{PyY}_5\text{Me}_2)_4\text{M}_4\text{Re}(\text{CN})_7]^{5+}$  ( $\text{M} = \text{Co}$  (**6**),  $\text{Ni}$  (**7**),  $\text{Cu}$  (**8**)) and  $[(\text{Py}_5\text{Me}_2)_4\text{Cu}_4\text{Re}(\text{CN})_7]^{4+}$  (**9**) [4]. The molecular structure of these heterometallic cations is similar to the cross-like organization of **4** and **5** (Figure 2a). Unlike complex **4**, an intramolecular reduction process ( $\text{Co}^{\text{II}} \rightarrow \text{Re}^{\text{IV}}$ ) takes place during a formation of the  $\text{Co}^{\text{II}}_4\text{Re}^{\text{IV}}$  core resulting in a  $\text{Co}^{\text{II}}_3\text{Co}^{\text{III}}\text{Re}^{\text{III}}$  species. Nevertheless, for the  $\text{Cu}^{\text{II}}_4\text{Re}^{\text{IV}}$  moiety, a thermally induced reduction similar to **4** is also observed to afford a  $\text{Cu}^{\text{II}}_4\text{Re}^{\text{III}}$  moiety. However, such a reduction may be precluded at low temperatures. It should be noted that the one-electron reduction was registered during a slow diffusion of the reagents in the case of the reaction of  $(n\text{-Bu}_4\text{N})_3[\text{Re}(\text{CN})_7]$  with  $[\text{Cu}(\text{cyclam})\text{Cl}_2]$  [41]. However, no reductive process was observed when using the nickel(II) complex  $[\text{Ni}(\text{cyclam})\text{Cl}_2]$  as a high-spin partner [41].

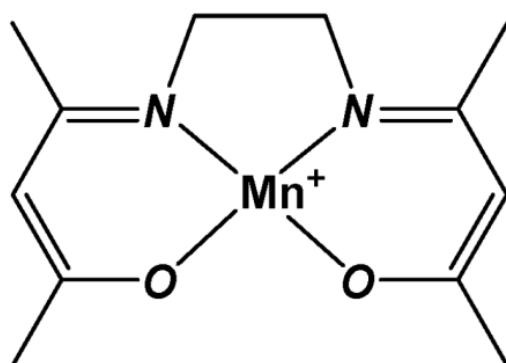
A simulation of the  $\chi T$ -plots for the pentanuclear compounds ( $\text{M}^{\text{II}} = \text{Mn}, \text{Ni}, \text{Cu}$ ) (Figure 2) was conducted using an exchange Hamiltonian of  $\hat{H} = -2J\hat{S}_{\text{Re}}(\hat{S}_{\text{M}(1)} + \hat{S}_{\text{M}(2)} + \hat{S}_{\text{M}(3)} + \hat{S}_{\text{M}(4)})$  [3,4]. The magnetic measurement data demonstrate intramolecular ferromagnetic exchange interactions (Figure 2), high mono-axial anisotropy, and slow magnetization relaxation in the  $\text{Ni}^{\text{II}}_4\text{Re}^{\text{IV}}$  (Figure 3, inset) and  $\text{Cu}^{\text{II}}_4\text{Re}^{\text{IV}}$  molecular cations. Next, the SMM characteristics ( $U_{\text{eff}} = 17 \text{ cm}^{-1}$  and  $\tau_0 = 1.4 \times 10^{-7} \text{ s}^{-1}$ ) were extracted from an Arrhenius plot made for **9**. Temperature dependencies of ac susceptibility measured on **8** also show a frequency-dependent signal at low temperatures, which prevented determination of the relaxation parameters [4].

### 3.3. Heterobimetallic Assemblies of $[\text{Re}^{\text{IV}}(\text{CN})_7]^{3-}$ and $\text{M}^{\text{III}}$ Schiff Base Complexes

According to the above studies on the preparation of heterobimetallic assemblies involving divalent  $3d$  metal ions, the latter can reduce  $\text{Re}(\text{IV})$  to form a diamagnetic metal-ligand  $[\text{Re}^{\text{III}}(\text{CN})_7]^{4-}$ . To avoid such a reduction process, it is necessary to use high-spin complexes containing  $3d$  metal in a higher oxidation state than +2. The most reasonable choice is to use  $\text{Mn}^{\text{III}}$  compounds with a spin ground state of  $S = 2$ . This choice is also suitable because to date, no whole family of  $\text{Mn}^{\text{III}}$  complexes with various  $\text{N}_2\text{O}_2$  Schiff bases (SB), condensation products of diamines, and derivatives of either salicylaldehyde or acetylacetonone has been synthesized and characterized [42,43]. Furthermore, the monocationic complexes  $[\text{Mn}(\text{SB})]^+$  have been widely used in the design of cyanidometallate-based molecular magnetic materials [9].

### 3.3.1. 3D Framework of $[\text{Mn}(\text{acacen})]_3[\text{Re}^{\text{III}}(\text{CN})_7]$ (**11**)

Employment of the least utilized molecular magnet complex in the engineering of LD,  $\text{Mn}(\text{acacen})\text{Cl}$  ( $\text{acacen} = N,N'$ -ethylenebis (acetylacetonylideneaminato)) (**10**), previously led to the preparation of anionic SCMs based on orbitally degenerate hexacyanidometallates ( $\text{Cation}$ )<sub>2</sub> $[\text{Mn}^{\text{III}}(\text{acacen})\text{M}^{\text{III}}(\text{CN})_6]$ ,  $\text{M}^{\text{III}} = \text{Fe}$  and  $\text{Os}$ ,  $\text{Cation} = \text{Et}_4\text{N}^+$  for iron, and  $\text{Ph}_4\text{P}^+$  for iron and osmium [14,21]. Note that the mixing of  $[\text{Mn}(\text{acacen})]^+$  (Scheme 3) with iron(III) cyanidometallate resulted in a family of heterobimetallic compounds of varying dimensionality (0D, 1D, and 2D), just changing the solvents and heating temperature and time [43]. However, the interaction of **1** with **10** in a ratio of 1:1 gave a 3D coordination polymer, i.e.,  $[\text{Mn}(\text{acacen})]_3[\text{Re}^{\text{III}}(\text{CN})_7]$  (**11**), regardless of the solvent (MeOH or  $\text{CH}_2\text{Cl}_2$ ) [44].



**Scheme 3.**  $[\text{Mn}(\text{acacen})]^+$ ; molecular magnetic unit used for the synthesis of  $\text{Mn}^{\text{III}}\text{Re}^{\text{IV}}$  assemblies.

#### Crystal Structure of $[\text{Mn}(\text{acacen})]_3[\text{Re}^{\text{III}}(\text{CN})_7]$

To understand the nature of magnetism of **11**, it is extremely important to analyze its crystal structure in more detail. The analysis of the crystal structure of **11** includes  $[\text{Mn}(\text{acacen})]^+$  and  $[\text{Re}(\text{CN})_7]^{3-}$  ions form a neutral 3D coordination polymer (Figures 1 and 2) with an independent unit comprising six  $\text{Mn}^{\text{III}}$  and two  $\text{Re}^{\text{III}}$  centers. All  $\text{Mn}^{3+}$  centers have a distorted octahedral environment comprised of two O and two N atoms in the equatorial plane of the  $\text{acacen}^{2-}$  ligand and two N atoms of CN linkers in axial positions of  $[\text{Re}(\text{CN})_7]^{3-}$  complexes. The  $\text{Mn}-\text{N}_{\text{CN}}$  distances in the range of 2.297(5)–2.388(5) Å, which is usual for Jahn–Teller distortion in  $\text{Mn}^{\text{III}}$  compounds, with each Re ion in a slightly distorted PBP environment. In fact,  $[\text{Re}(\text{CN})_7]^{3-}$  is much less distorted than its 4d equivalent,  $[\text{Mo}(\text{CN})_7]^{4-}$ , in  $\text{Mn}_2(\text{H}_2\text{O})_5\text{Mo}(\text{CN})_7 \cdot 4\text{H}_2\text{O}$  [27] and  $\text{Mn}_4\text{L}_4(\text{H}_2\text{O})_2(\text{Mo}(\text{CN})_7)_2$  [45], but the distortion of the Re polyhedron of **11** is comparable with that of molybdenum in the  $\text{Mn}^{\text{II}}_2\text{Mo}^{\text{III}}$  framework [28]. The Re–C average distance is 2.106(19) Å, which is comparable to that which was established for  $(n\text{-Bu}_4\text{N})_3[\text{Re}(\text{CN})_7]$  (2.09(2) Å) [38]. Six cyanides of the  $[\text{Re}(\text{CN})_7]^{3-}$  unit bond to six  $[\text{Mn}(\text{acacen})]^+$  cations, making a framework with a distorted cubic topology (Figures 4 and 5). The framework structure of **11** is a singular example of 3D heterobimetallic polymer constructed from a  $[\text{Mn}^{\text{III}}\text{SB}]^+$  unit and a polycyanidometallate, which can be explained by the relatively small size of  $[\text{Mn}(\text{acacen})]^+$  compared to the  $\text{Mn}^{\text{III}}$  complexes of *salen*-based SB and the larger size of the 5d metal cyanide complex. It is also probable that the PBP arrangement of the metalloligand is favorable for the formation of a 3D polymer. We found no published examples of the related bimetallic compounds based on octahedral cyanidometallates.

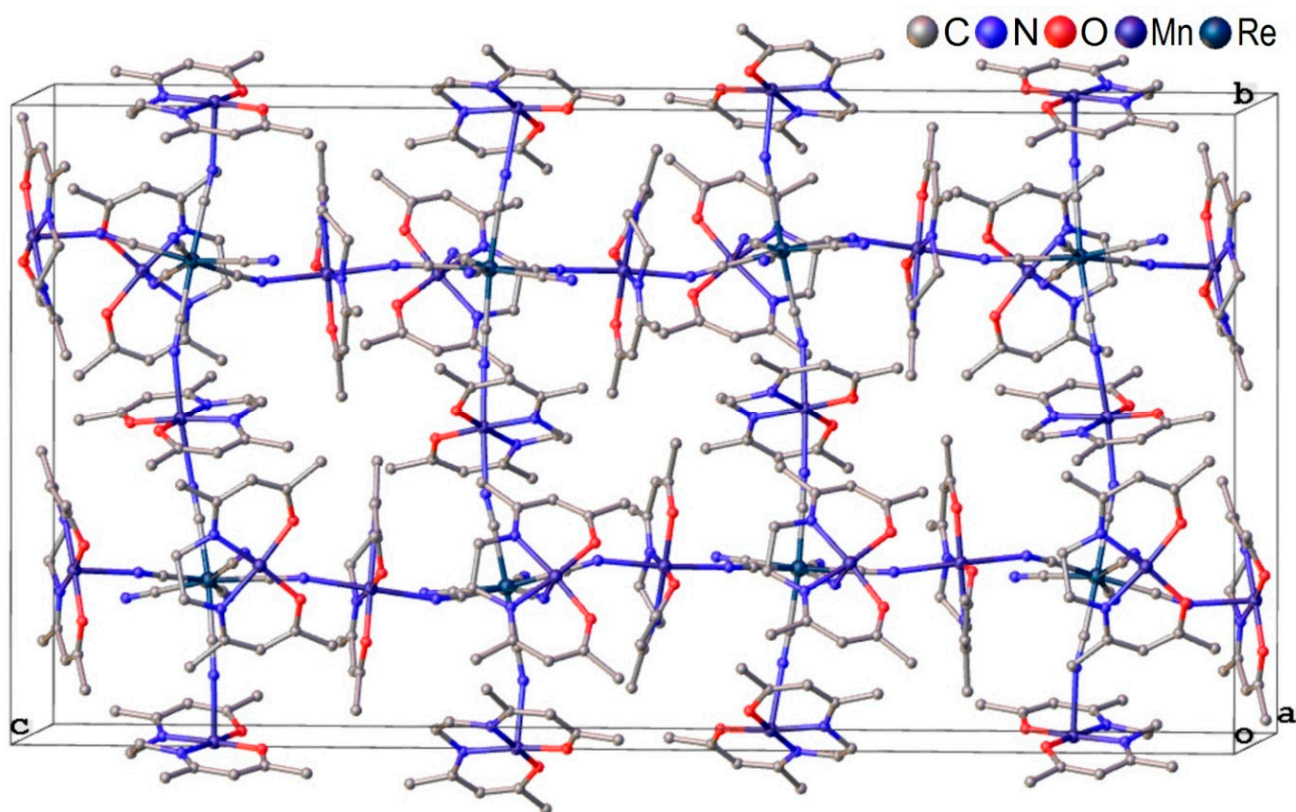


**Figure 4.** Unit cell of **11** ( $P2_1/n$ ,  $a = 10.6492(3) \text{ \AA}$ ,  $b = 21.8027(5) \text{ \AA}$ ,  $c = 41.839(1) \text{ \AA}$ ,  $\beta = 92.570(1)^\circ$ ,  $V = 9704.5(4) \text{ \AA}^3$ ) projected on the  $bc$  plane. The apical axes of  $[\text{Re}(\text{CN})_7]^{3-}$  units (slightly distorted PBPBs) are oriented along the  $b$  axis, suggesting that  $b$  is the easy magnetic axis (see the text) [44].

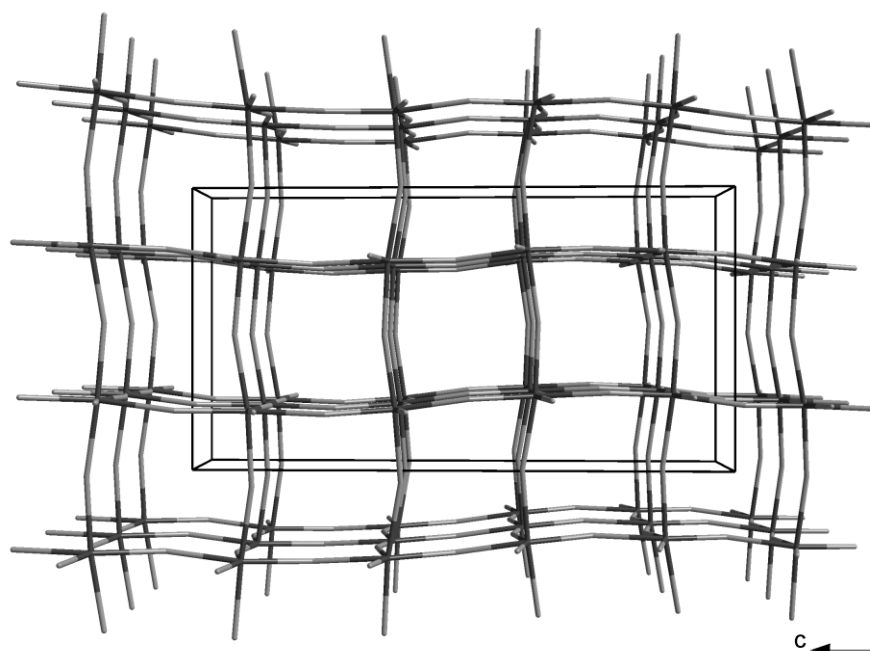


**Figure 5.** Schematic presentation of the 3D network with distorted cubic topology in **11** (along the 100 direction). Reproduced with permission from ref. [44]. © 2022 American Chemical Society.

In order to interpret the magnetic behavior of a heterometallic system, it is useful to analyze the mutual arrangement of structural elements in the crystal of a compound

under study. Thus, based on the structure of **11**, it can be assumed that the direction along the *b* axis is an easy magnetization axis, as the apical axes, CN–Re–CN, are located in this direction, despite their small slope relative to each other (Figure 4). Owing to the pseudocubic structure of **11**, all the Jahn–Teller axes of the Mn<sup>III</sup> complexes in parallel Re–Mn–Re–Mn chains are also mutually inclined [44].

Because one of the cell angles is slightly greater than 90° and the space group is different from  $P\bar{1}$ , the directions of the hard and easy magnetization axes do not coincide with other crystallographic axes, as illustrated in Figure 6 [44].

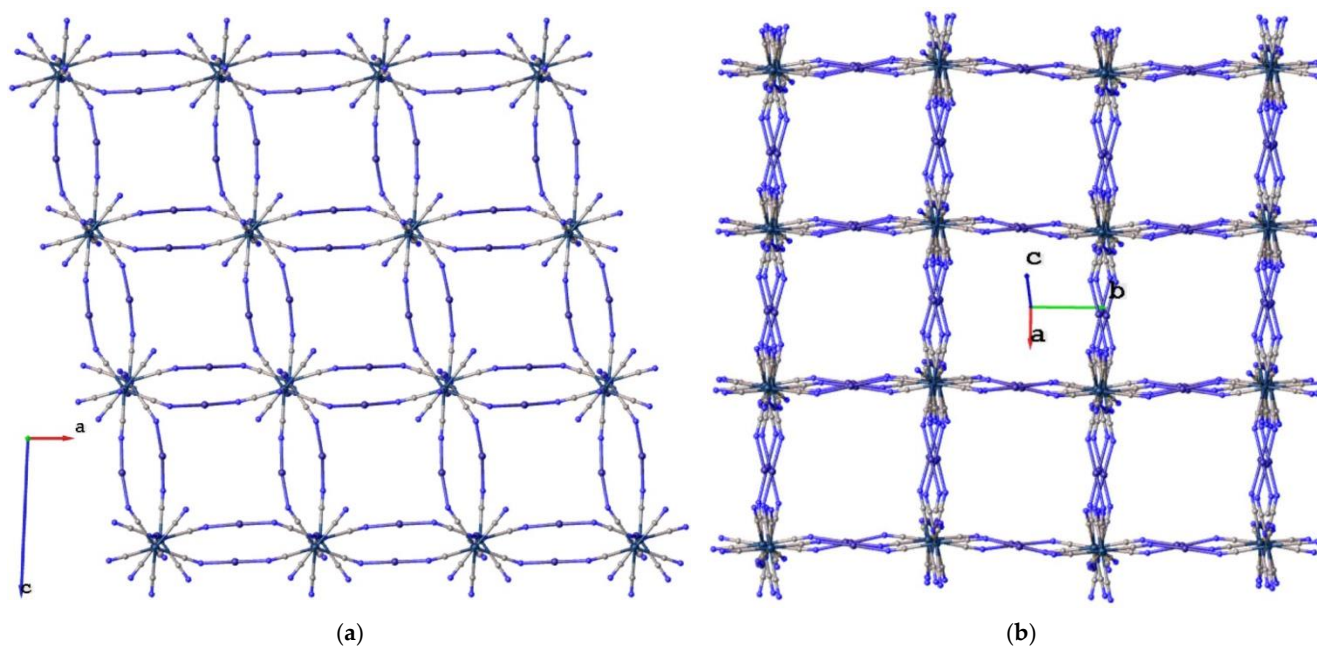


**Figure 6.** Different views for the structure of **11**: (a) along the *b* axis (010); (b) projection on the 101 plane.

#### Magnetic Studies of Polycrystalline Samples

The high-temperature  $\chi T$  vs. *T* graphic of a polycrystalline **11** is presented in Figure 7. At 300 K, the observed value of 9.55 matches the theoretical value of 9.51 cm<sup>3</sup> K mol<sup>−1</sup> for one Re<sup>V</sup> (*S* = 1/2, *g* = 2.33) [38] and three Mn<sup>III</sup> (*S* = 2) uncoupled spins. Beginning from 300 K, the plot falls progressively and comes to a shallow minimum of 9 cm<sup>3</sup>·K·mol<sup>−1</sup> at 80 K (Figure 7, inset 1) [44]. Such a conduct of  $\chi T$  indicates ferrimagnetic interactions between the Mn<sup>III</sup> and Re<sup>V</sup> ions. The data for the temperature region of 100–300 K shows that  $\chi$  follows the Curie–Weiss law  $C = 9.86$  cm<sup>3</sup> K mol<sup>−1</sup> and with  $\Theta = -9.8$  K, confirming an entire antiferromagnetic character of exchange couplings in **11**. Below 50 K,  $\chi T$  increases and achieves a sharp maximum at 13 K, attesting to a magnetic phase transition in **11**. Analogous behavior was previously reported in a Mn<sub>2</sub>(H<sub>2</sub>O)<sub>5</sub>Mo(CN)<sub>7</sub>·4H<sub>2</sub>O framework containing an isoelectronic PBP [Mo<sup>III</sup>(CN)<sub>7</sub>]<sup>4−</sup> unit [27].

A metamagnetic transition in **11** occurs at 2 K in a field of approximately 5 kOe (see insert 2 of Figure 7). This compartment emerges at temperatures below 13 K, as evidenced by *M* vs. *H* plots collected at different temperatures (Figure 8a). The *ac* susceptibility data obtained for several frequencies do not confirm a frequency dependence (Figure 8b), suggesting a phase transition at the Néel temperature, i.e., *T*<sub>N</sub> = 13 K, below which the framework becomes a metamagnet.

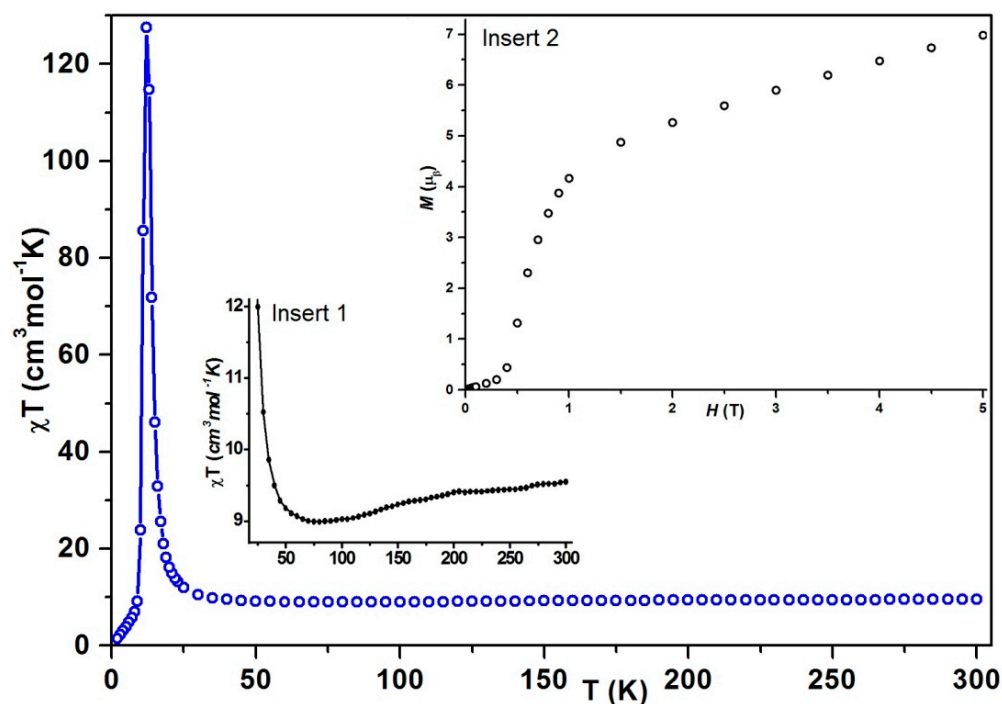


**Figure 7.** Magnetic data for a polycrystalline sample of **11**: the temperature dependence of  $\chi T$  (blue, solid line) registered at  $H = 5$  kOe. (insert 1: zoom of the  $\chi T$  plot) [44]. Insert 2: the field dependence of magnetization at 2 K [44].

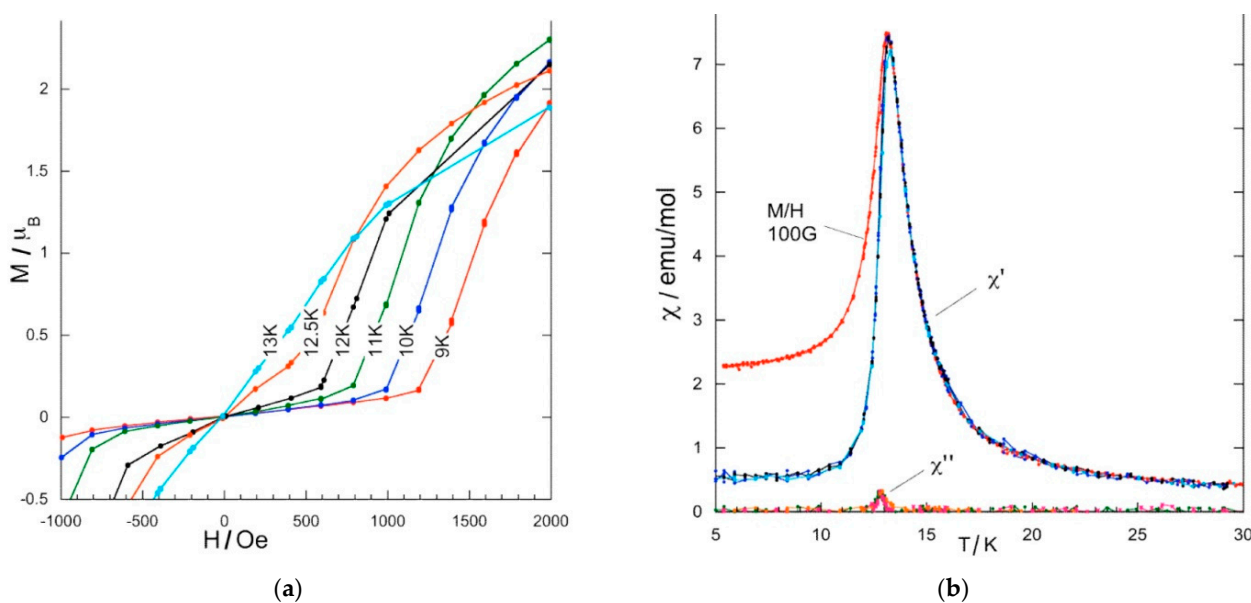


**Figure 8.** Magnetic data for a powder sample of **11**: (a)  $M$  vs.  $H$  plots at different temperatures closed to  $T_N$ ; (b) the temperature dependencies of  $dc$  susceptibility at 100 Oe and the  $\chi'$  and  $\chi''$  parts of the  $ac$  susceptibility obtained with  $H_{dc} = 1$  Oe at 0.57, 5.7, and 57 Hz. Reproduced with permission from ref. [44]. © 2022 American Chemical Society.

The  $ac$  data of **11** obtained in a field of 1 Oe for different frequencies do not demonstrate a frequency dependence (Figure 8b), with a small imaginary part ( $\chi''$ ) and showing only a pimple at the location of the  $\chi'$  peak. Such a phenomenon at 13 K is additional proof of a phase transition taking place. The  $dc$  magnetic data registered in a field of 100 Oe indicate that the maximum susceptibility occurs at a Néel temperature of  $T_N = 13$  K, below which the system exhibits metamagnetic behavior [44].

In spite of the absence of ferromagnetic order, hysteresis was observed for a powder of **11** at 200 mK (Figure 9a). The blue plot shows the initial magnetization, the latter with magnetization jumps or avalanches when the field attains a critical value of approximately 1.3 T and ~2 T; the hysteresis is closed only when the field is greater than 4 T [44]. The full hysteresis of **11** displays a very high coercive field of ~1 T. Furthermore,  $M$  does not saturate at 200 mK in fields up to 8 T and exhibits a linear dependence with high fields, which is typical for strongly anisotropic systems [44]. The maximum obtained value of  $M$  is  $\sim 8.8 \mu_B$ . This is far from the theoretical expectation ( $13\mu_B$  or  $11\mu_B$  for ferro- or antiferromagnetic interaction between the paramagnetic centers). Furthermore, at  $H = 0$ ,  $M$  reaches  $\sim 3.6 \mu_B$ , which is significantly less than half of the saturation value, attesting to uniaxial anisotropy. This suggests a spin canting arising from the noncollinearity of both the  $[\text{Re}(\text{CN})_7]^{3-}$  apical axes and the Jahn–Teller  $[\text{Mn}(\text{acacen})]^+$  axes caused by the pseudo-cubic organization of the 3D framework [44].

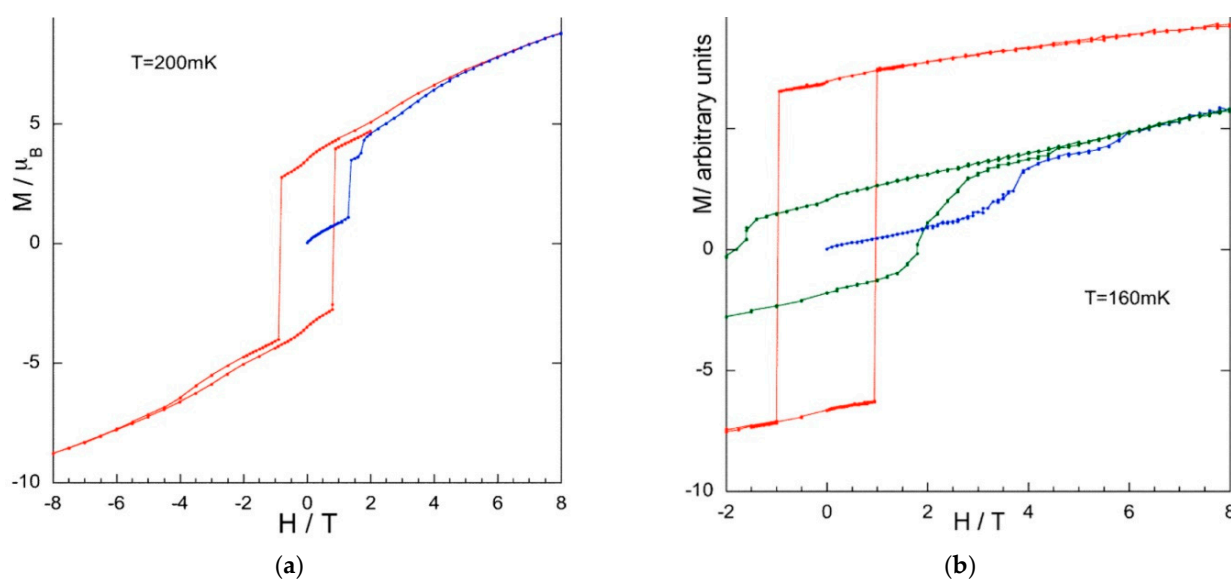


**Figure 9.** (a) Hysteresis measured on a powder sample of **11** at 200 mK; blue data points represent the initial magnetization [44]; (b) Hysteresis loops collected at 160 mK on a single crystal of **11** along the  $b$  axis (red) and  $c$  axis (green) and the initial magnetization along the  $b$  axis (blue) [44]. Reproduced with permission from ref. [44]. © 2022 American Chemical Society.

#### Magnetic Studies on a Single Crystal

To probe the anisotropic compartment of compound **11**, a magnetic investigation was carried out on a single crystal. The hysteresis loops measured at 160 mK along the  $b$  ( $\perp 010$ ) and  $c$  ( $\perp 100$ ) directions, as well the initial magnetization curve for the  $c$  direction, are presented in Figure 9b [44]. The initial magnetization curve demonstrates two different fields with changes in magnetization at 4 and 6 T [44]. Alternatively, for the direction,  $b$  ( $\perp 010$ ), at 1 T a step of magnetization takes place, with  $M$  not reaching a saturation value at 8 T and 160 mK. This indicates that the spins are not reciprocal along this direction. The easy magnetization axis ( $b$ ) coincides with a preferred direction of the apical axes of the  $[\text{Re}(\text{CN})_7]^{3-}$  pentagonal bipyramids (Figures 4–6), whereas the second orientation is in their equatorial plane ( $a$  or  $c$ ) [44].

In summary, the magnetic investigation shows that the  $[\text{Mn}(\text{acacen})]_3[\text{Re}^{\text{III}}(\text{CN})_7]$  undergoes a magnetic order of a complex character below 13 K, exhibiting metamagnetism and strong anisotropy relative to those observed in  $\text{Mn}^{\text{II}}_2[\text{Mo}(\text{CN})_7]$  frameworks, in which  $\text{Mn}^{2+}$  is magnetically isotropic. Further, we show that these unusual magnetic properties are due to an extremely sophisticated interplay of anisotropic spin coupling of  $\text{Mn}^{\text{III}}\text{-CN-Re}^{\text{IV}}$  linkages and single-ion ZFS anisotropy of  $[\text{Mn}(\text{acacen})]^+$  complexes in the 3D network of **11** [44].

### Theoretical Analysis of Anisotropic Spin Coupling in Re–CN–Mn Binding

The previously elaborated the superexchange theory to describe the anisotropic spin coupling between high-spin  $\text{Mn}^{\text{II}}$  ions ( $S = 5/2$ ) cyanide bonded to  $[\text{Mo}^{\text{III}}(\text{CN})_7]^{4-}$  with an ideal PBP polyhedron was used to find the exchange parameters in **11**, as heptacyanido-molibdate(III) is isoelectronic to  $[\text{Re}(\text{CN})_7]^{3-}$  ( $nd^3$ -configuration) [1]. For the regular  $D_{5h}$  symmetry or slightly distorted PBP coordination polyhedron of the  $[\text{Re}(\text{CN})_7]^{3-}$ , the spin coupling in the bent and distorted Re–CN–Mn fragments is described by the same uniaxial anisotropic spin Hamiltonian,  $-J_{xy}(S_{\text{Mn}}^x S_{\text{Re}}^x + S_{\text{Mn}}^y S_{\text{Re}}^y) - J_z S_{\text{Mn}}^z S_{\text{Re}}^z$ , independent of the local symmetry of  $[\text{Mn}^{\text{III}}\text{SB}]^+$  complexes [44]. This means that the lowering of symmetry in Re–CN–Mn groups does not break up the total uniaxial symmetry of the spin Hamiltonian if the Re PBP remains ideal or only slightly distorted [44]. The numerical microscopic calculations of anisotropic exchange parameters  $J_z$  and  $J_{xy}$  for all Re–CN–Mn fragments in structure of **11** were performed in terms of a many-electron superexchange theory [44].

Consequently, it was demonstrated that in the case of a small distortion in the  $\text{Re}^{\text{IV}}$  bipyramid, L of  $[\text{Re}(\text{CN})_7]^{3-}$  is not quenched, and the ground state wave functions are almost the same as those in an ideal  $D_{5h}$  polyhedron, as the splitting energy of  ${}^2\Phi_{\pm}$  is much less than the spin-orbit splitting energy  $\approx 2400 \text{ cm}^{-1}$  [44]. Hence, the application of the regular  $D_{5h}$  geometry of  $[\text{Re}(\text{CN})_7]^{3-}$  is a satisfying approach in theoretical modeling of anisotropic spin coupling in compound **11**. The dependence of  $J_z$  and  $J_{xy}$  on the C–N–Mn bond angle for all 12 nonequivalent Re–CN–Mn exchange-coupled pairs found in the crystal structure of **11** was calculated within the framework of the theory of many-electron superexchange [44]. The calculation results reveal a very complex interplay of anisotropic spin coupling between apical and equatorial Re–CN–Mn fragments in **11**. Although in all pair, the anisotropic spin Hamiltonian (Equation (1)) maintains an axial symmetry with the anisotropy  $z$  axis parallel to a polar axis of the  $\text{Re}^{\text{IV}}$  PBP,  $J_z$  and  $J_{xy}$  parameters diverge significantly from pair to pair [44]. The exchange anisotropy for the apical pairs possesses a pronounced Ising-like character ( $|J_z| > |J_{xy}|$ ), whereas the spin coupling in equatorial pairs is close to isotropic, with a small  $xy$  contribution [44].

$$\widehat{H}_{\text{eff}} = -J_{xy}(S_{\text{Mn}}^x S_{\text{Re}}^x + S_{\text{Mn}}^y S_{\text{Re}}^y) - J_z S_{\text{Mn}}^z S_{\text{Re}}^z \quad (1)$$

Using the largest parameters determined by microscopic calculations— $J_z = -18$  and  $J_{xy} = -8 \text{ cm}^{-1}$  for the apical Re–CN–Mn fragment and  $J_z = -19$  and  $J_{xy} = -20 \text{ cm}^{-1}$  for the equatorial groups—sufficiently accurate agreement  $> 30 \text{ K}$  was achieved between the experimental and simulated  $\chi T$  plots ( $D = -4.0 \text{ cm}^{-1}$ ,  $E = 0$ , and  $g_{\text{Mn}} = 2.03$  for  $\text{Mn}^{\text{III}}$  were fixed), (Figure 10a), with the minimum in the  $\chi T$  graph around  $75 \text{ K}$  well-reproduced. The minimum is a result of a peculiar configuration of the theoretical spin-energy spectrum of **11** [44]. Uniaxial anisotropic antiferromagnetic spin coupling of alternating  $S_{\text{Re}} = 1/2$  and  $S_{\text{Mn}} = 2$  spins tends to stabilize collective spin states with large  $M_S$  projection on the polar  $z$  axis of the Re site (Figure 10b). In the middle energy range  $\sim 60 \text{ cm}^{-1}$ , there is a low density of energy levels, which are represented by spin states with reduced  $M_S$  spin projection, in contrast to the upper spin states corresponding the high  $M_S$  projection (Figure 10b). Therefore, at low temperatures, the thermal population of low-lying spin states with large  $M_S$  results in a robust increase in susceptibility below  $25 \text{ K}$ , whereas the subsequent thermal population of the next excited spin states first results in a flat minimum at moderate temperatures and then a steady increase in  $\chi T$  at higher temperatures (Figure 10a) [44].

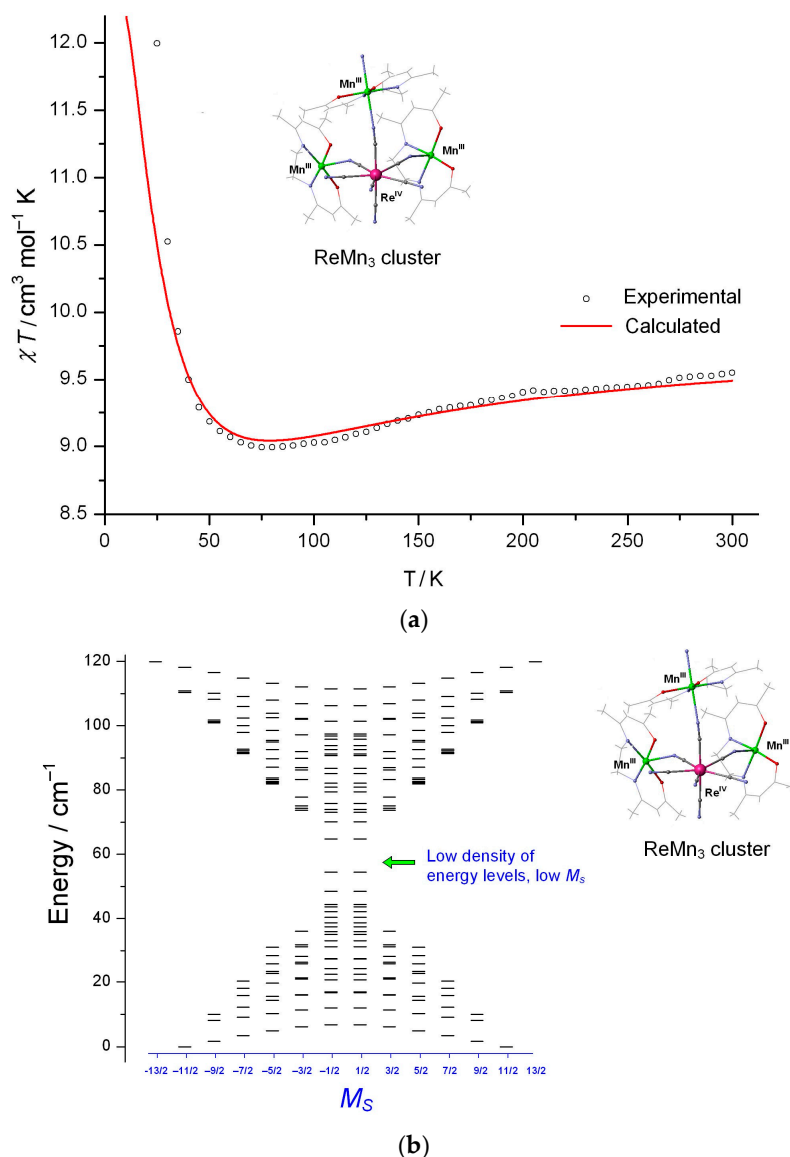


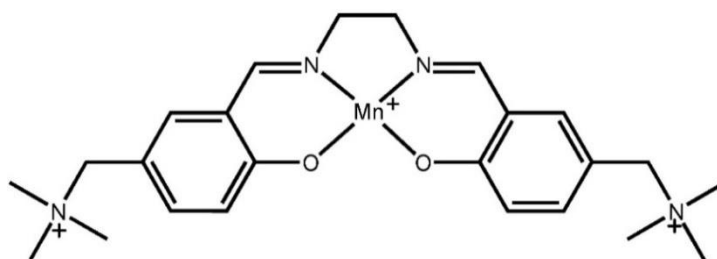
**Figure 10.** (a) The experimental (circles) and simulated  $\chi T$  curve for the isolated  $\text{ReMn}_3$  cluster (red line) of **11** above  $T_N = 13$  K. Calculations were performed with  $J_z = -18$ ,  $J_{xy} = -8 \text{ cm}^{-1}$ ,  $J_z = -19$ ,  $J_{xy} = -20 \text{ cm}^{-1}$  for the apical and equatorial pairs, respectively;  $D = -4.0 \text{ cm}^{-1}$ ,  $E = 0$  (ZFS parameters for  $\text{Mn}^{\text{III}}$  ions),  $g_z = 3.66$  and  $g_x = g_y = 1.59$  for  $[\text{Re}(\text{CN})_7]^{3-}$ , and  $g_{Mn} = 2.03$  [44]. (b). Calculated spin-energy spectrum of the  $\text{ReMn}_3$  cluster. Low density of energy levels in the middle range of the energy spectrum (represented by spin states with a low  $M_S$  projection) is responsible for a flat minimum in the  $\chi T$  curve. Reproduced with permission from ref. [44]. © 2022 American Chemical Society.

### 3.3.2. LD Neutral Assemblies $[\text{Mn}(\text{SB}^{2+})\text{Re}(\text{CN})_7] \cdot x\text{H}_2\text{O}$

Electroneutrality is an important contribution to the self-assembly of molecular building blocks in heterometallic coordination compounds.  $\text{Mn}^{\text{III}}$  complexes with Schiff bases of both the *acacen* and *salen* type generally have a charge of +1, whereas heptacyanidorhenate is a trianion. Hence, to obtain a 1D alternating  $-\text{Re}-\text{CN}-\text{Mn}-\text{NC}-\text{Re}-\text{CN}-$  polymer (1:1 ratio) two additional noncoordinating cations are required. This approach was fruitful for hexacyanide complexes of  $\text{Fe}^{\text{III}}$  and  $\text{Os}^{\text{III}}$  [14,21]. However, when using  $\text{PPN}^+$  and  $\text{Ph}_4\text{P}^+$ , layered compounds were obtained, which will be described in the last part of this review.

Previously, a family of neutral magnetic wires with a 1:1  $\text{Mn}^{\text{III}}$ /cyanidometallate ratio were obtained and 0D species:  $[\text{Mn}^{\text{III}}(\text{SB}^{2+})\text{M}^{\text{III}}(\text{CN})_6] \cdot 4\text{H}_2\text{O}$  ( $\text{M}^{\text{III}} = \text{Fe}, \text{Cr}, \text{Mn}$ ) [20]

and  $[\text{Mn}^{\text{III}}(\text{SB}^{2+})(\text{H}_2\text{O})\text{W}^{\text{V}}(\text{CN})_8] \cdot 8\text{H}_2\text{O}$ , as well as  $[\text{Mn}(\text{SB}^{2+})(\text{H}_2\text{O})\text{W}^{\text{V}}(\text{CN})_8] \cdot 5\text{H}_2\text{O}$  [15], where  $[\text{Mn}^{\text{III}}(\text{SB}^{2+})]^{3+}$  is a trication (see Scheme 4). Therefore, in order to prepare the neutral LD species containing  $[\text{Re}^{\text{IV}}(\text{CN})_7]^{3-}$ , the same methodology was employed using the same starting complex,  $[\text{Mn}(\text{SB}^{2+})(\text{H}_2\text{O})_2](\text{ClO}_4)_3 \cdot \text{H}_2\text{O}$ , as a source of high-spin molecular units. When an acetonitrile solution of  $(\text{Bu}_4\text{N})_3[\text{Re}(\text{CN})_7]$  is layered on an aqueous solution of a manganese(III) complex, large, dark crystals of a 1D polymer (**12**) are formed [46]. Compound **12** can also be synthesized as a crystalline powder by the gentle addition of a solution of a  $\text{Mn}^{\text{III}}$  complex to a solution of cyanidometallate. The slow recrystallization of compound **12** powder in aqueous medium resulted in the formation in a small amount of crystals of the binuclear complex  $[\text{Mn}(\text{SB}^{2+})(\text{H}_2\text{O})\text{Re}(\text{CN})_7] \cdot 2\text{H}_2\text{O}$  (**13**).



**Scheme 4.** Molecular structure of triply charged *salen*-type  $[\text{Mn}(\text{SB}^{2+})]^{3+}$ .

#### Crystal Structure Description

SCXRD showed that the assembly **13** has a 0D structure, whereas **12** is a 1D chain polymer. Molecular views of the repeating unit in the complex  $\{[\text{Mn}(\text{SB}^{2+})\text{Re}(\text{CN})_7]\}_n$  (**12**) and an asymmetric unit of  $[\text{Mn}(\text{SB}^{2+})(\text{H}_2\text{O})\text{Re}(\text{CN})_7] \cdot 2\text{H}_2\text{O}$  (**13**) are presented in Figure 11. Both compounds are neutral bimetallic assemblies consisting of one  $[\text{Re}(\text{CN})_7]^{3-}$  anion and one cation ( $[\text{Mn}(\text{SB}^{2+})]^{3+}$  for **12** or  $[\text{Mn}(\text{SB}^{2+})(\text{H}_2\text{O})]^{3+}$  for **13** [46].

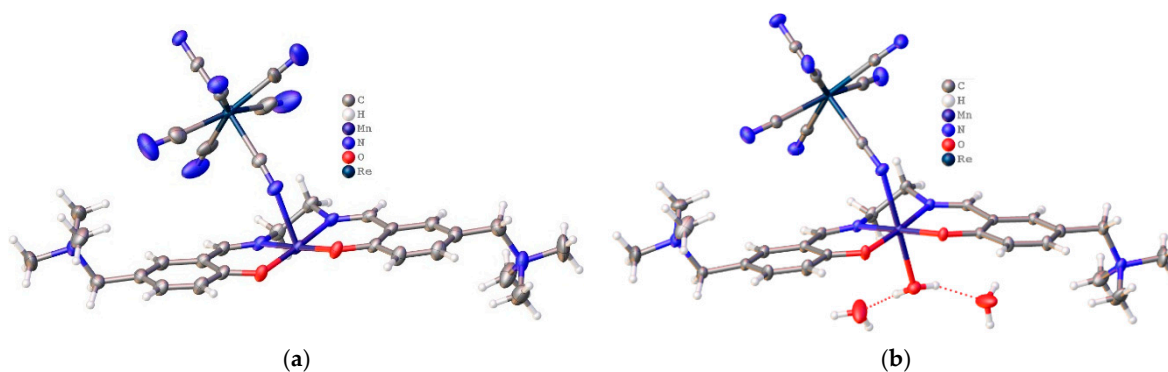


**Figure 11.** (a) The repeating unit in the chain of **12** (solvent water molecules are omitted) and (b) the molecular unit in **13**. ORTEP diagrams were generated with 50% probability thermal ellipsoids [46].

In both compounds, a slightly distorted PBP coordination environment of the rhenium ion involves seven cyanides. In fact,  $[\text{Re}(\text{CN})_7]^{3-}$  is considerably less deformed than its iso-electronic equivalent,  $[\text{Mo}(\text{CN})_7]^{4-}$  [26–28]. The Re–C distances are close to those for  $(\text{Bu}_4\text{N})_3[\text{Re}(\text{CN})_7]$  [38]. The geometry of the manganese atom is a tetragonal bipyramid typical for the Jahn–Teller elongation.

The  $\text{Mn}-(\text{N}\equiv\text{C})_{\text{axial}}$  angle departs noticeably from  $180^\circ$  and equates to  $144.2^\circ$  and  $145.1^\circ$  for **12** and **13**, correspondingly, close to the value of  $144.4^\circ$  for  $[\text{Mn}(\text{SB}^{2+})\text{Fe}(\text{CN})_6]$  [20]. Such a trend is typical for cyanide-based  $\text{Mn}-\text{M}(\text{CN})_n$  complexes [9,43,47–52]. Nevertheless, for the coordination compounds of  $\text{SB}^{2+}$ , which is a sterically demanding ligand, this angle is particularly deviated from  $180^\circ$  [47]. For example, for a much less bulky SB complex, such as  $[\text{Mn}(\textit{acacen})]^+$ , the value of this angle for the  $\text{Re}^{\text{IV}}-\text{Mn}^{\text{III}}$  system fluctuates within the bounds of  $152.9$ – $163.7^\circ$  [9,43,44]. Furthermore, the  $\text{Mn}-(\text{N}\equiv\text{C})$  angle is  $162.6$  and  $160.1^\circ$

in 0D complexes  $[\text{Mn}(\text{MeSB}^{2+})(\text{H}_2\text{O})\text{Fe}(\text{CN})_6]$  [47] and  $[\text{Mn}(\text{SB}^{2+})(\text{H}_2\text{O})\text{W}(\text{CN})_8]$  [15], respectively. Analysis of the geometric parameters in heterometallic compounds is extremely important. For example, the greater the deviance from  $180^\circ$  in the  $\text{Mn}-(\text{N}\equiv\text{C})-$  fragment, the greater the contribution of sigma binding to the  $\text{Mn}-\text{Re}$  exchange interaction.

Contrary to the  $\{\text{Mn}^{\text{III}}(\text{SB})\text{M}(\text{CN})_m\}$  compounds—where SB is a *salen*-type ligand, for which a dimerization of the  $\text{Mn}^{\text{III}}(\text{SB})$  fragments is fairly common [9]—the trications  $[\text{Mn}(\text{SB}^{2+})\text{H}_2\text{O}]^{3+}$  in the 0D complexes involving hexa- or heptacyanidometallates are not dimerized in a crystal due to the *trans* location of the  $[\text{Me}_3\text{N}^+\text{CH}_2]$  groups relative to the  $\text{SB}^{2+}$ -ligand plane [46,47], whereas the molecules of  $[\text{Mn}(\text{SB}^{2+})(\text{H}_2\text{O})\text{W}(\text{CN})_8]$  [15] are dimerized due to hydrogen bonding,  $\pi-\pi$  stacking, and nonvalent  $\text{CN} \dots \text{H}$  interactions of the  $[\text{Me}_3\text{N}^+\text{CH}_2]$  groups, which are *cis* located relative to each other.

In a crystal, the chains of **12** (Figure 12) are connected to the layers through a system of hydrogen bonds. Compound **13** possesses a pseudo-3D structure, as it also has the developed system of hydrogen bonds. Coordinated to the Mn center, a water molecule participates in the formation of a 1D system of hydrogen bonds that connects the discrete binuclear species in the chains (Figure 13), which are then bounded into the layers interconnected by the sufficiently short contacts  $\text{C}\equiv\text{N} \dots \text{H}-\text{C}$  and  $\text{C}-\text{O} \dots \text{H}-\text{C}$  of  $\sim 2.5 \text{ \AA}$  [46].

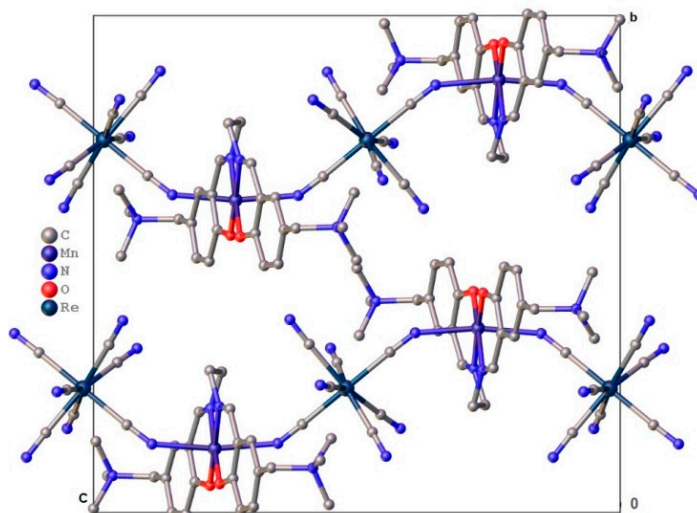


**Figure 12.** View of the chains in **12** projected along the *a* axis. Hydrogen atoms and interstitial water molecules are omitted for clarity [46].

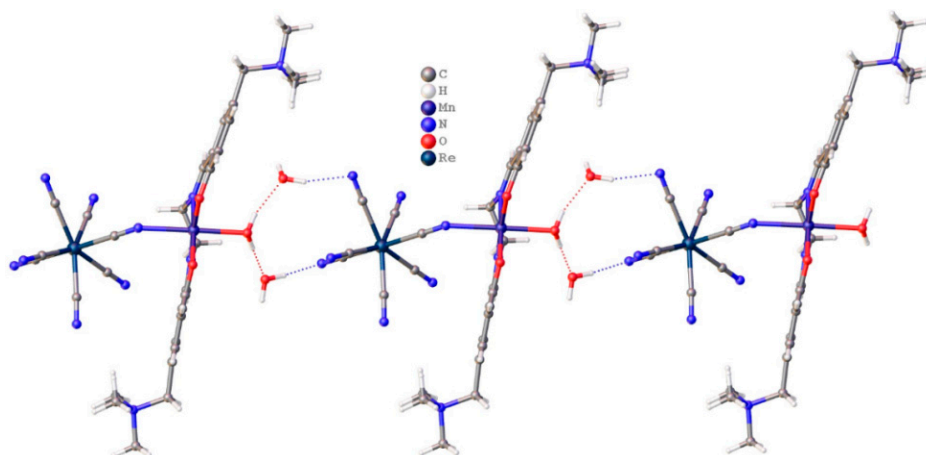


**Figure 13.** The 1D motif formation in **13**. A view along the *b* axis [46].

### Static Magnetic Behaviors

The temperature dependence of the *dc* molar  $\chi T$  for the polycrystalline sample of **12** is presented in Figure 14. At 300 K, the  $\chi T$  value of 3.68 is very close to the 3.60  $\text{emu K mol}^{-1}$  expected for one  $\text{Mn}^{\text{III}}$  ( $S = 2, g = 2.03$ ) [44] and one  $\text{Re}^{\text{IV}}$  ( $S = 1/2, g = 2.33$ ) [38] as nonintersected spins. The  $\chi T$  decreases slightly, reaching a shallow minimum of 3.28  $\text{emu K mol}^{-1}$  at  $\sim 75$  K. This comportment of  $\chi T$  is typical of antiferromagnetic coupling of the  $\text{Mn}^{\text{II/III}}$  and  $\text{Re}^{\text{IV}}$  ions within the chains [44,52]. Below 50 K,  $\chi T$  increases, reaching a maximum of 9.30  $\text{emu}\cdot\text{K}\cdot\text{mol}^{-1}$  at  $\sim 5$  K before falling to 6.48  $\text{emu K mol}^{-1}$  at 2 K.

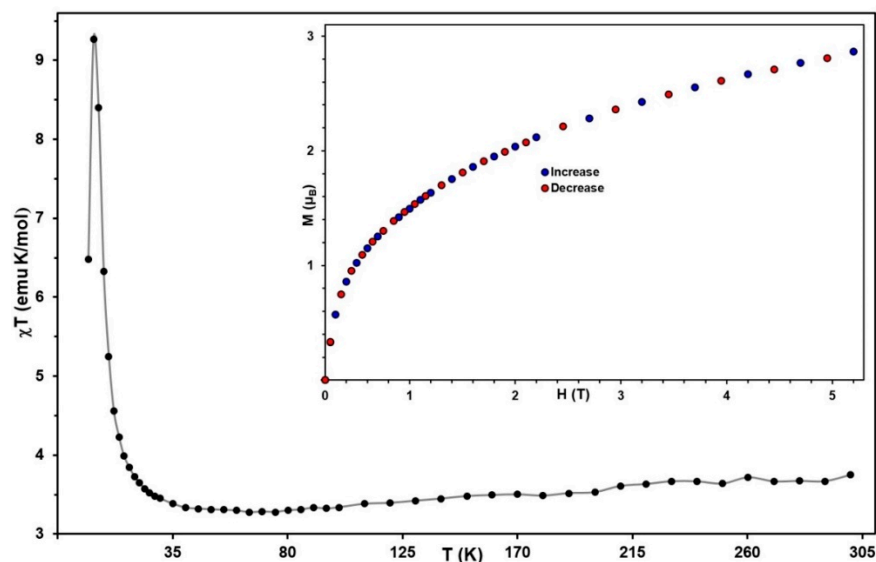


**Figure 14.** Magnetic *dc* plots for **12**. Temperature dependence of  $\chi T$  at  $H = 1000$  Oe (solid line). Inset: magnetization versus the field at  $T = 2$  K [46].

The  $M(H)$  plot of **12** registered at 2 K demonstrates a full magnetization reversibility (Figure 14, inset). The  $M$  value reached at 50 kOe is 2.86  $\mu_B$  per  $\text{Mn}^{\text{III}}\text{-Re}^{\text{IV}}$  units, which is far from 5  $\mu_B$  (theoretical value consistent with five unpaired electrons) [46]. The calculated magnetic field saturation ( $H_A$ ) for **12** is approximately 151 kOe, being much greater than the values of 100, 108, and 120 kOe established for  $[(\text{SB}^{2+})(\text{Cr}/\text{Fe})(\text{CN})_6]$  [20] and  $[\text{Mn}^{\text{III}}(\text{acacen})\text{Fe}^{\text{III}}(\text{CN})_6]^{2-}$  [21], respectively.

The magnetic behavior of **13** was studied on a sample consisting of the crystals manually sorted and scrupulously separated from the possible powder impurities of the 1D precursor [46]. The magnetic properties of **13** (Figure 15) are somewhat similar to those of **12**; the  $\chi T$  temperature plot also shows a sharp maximum, and the shape of the graphics for  $M(H)$  is comparable to that for **12**. Moreover, the  $\chi T$  value of 3.68  $\text{emu}\cdot\text{K}\cdot\text{mol}^{-1}$  at 300 K practically coincides with that registered for **12**. Furthermore, unlike **13**,  $\chi T$  increases slowly, indicating a ferromagnetic interaction between the spins, with approximately 3.85  $\text{emu}\cdot\text{K}\cdot\text{mol}^{-1}$  at 70 K, after which the  $\chi T$  values begin to increase, reaching a peak of 8.21  $\text{emu}\cdot\text{K}\cdot\text{mol}^{-1}$  at 5 K and then dropping abruptly [46]. The existence of the peak on the  $\chi T$  curve at 5 K is unexpected for a 0D species, as no peak was found in  $\chi T(T)$  of the related compounds:  $[\text{Et}_4\text{N}]_2[\text{Mn}(\text{saldmen})(\text{H}_2\text{O})\text{Fe}(\text{CN})_6]$  (saldmen is  $N,N'$ -(1,1-dimethylethylene)bis(salicylideneimine)) [53] and  $[\text{Mn}^{\text{III}}(\text{MeSB}^{2+})(\text{H}_2\text{O})\text{Fe}(\text{CN})_6]$  [47].

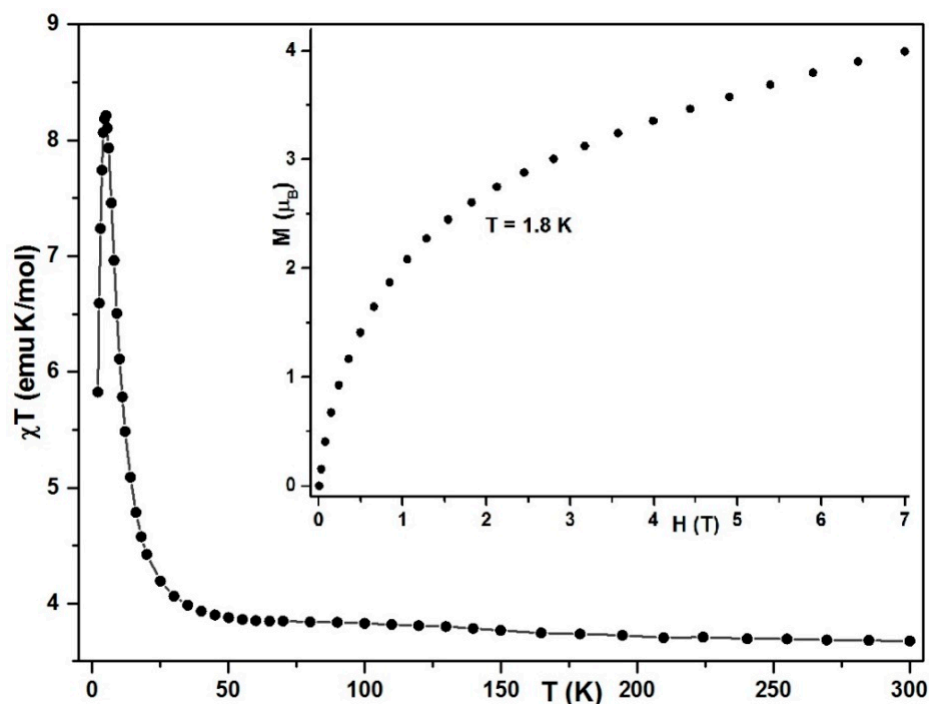


**Figure 15.** Magnetic dc plots for **13**. Temperature dependence of  $\chi T$  at  $H = 1000$  Oe (solid line). Inset: magnetization versus the field at  $T = 2$  K [46].

The  $M(H)$  plot for **13** is shown in Figure 15 (inset). Note the value of  $M$  of  $3.58 \mu_B$  for  $[\text{Mn}^{\text{III}}(\text{MeSB}^{2+})(\text{H}_2\text{O})\text{Fe}(\text{CN})_6]$  [47] at 50 kOe is close to the  $3.45 \mu_B$  of the binuclear complex  $[\text{Et}_4\text{N}]_2[\text{Mn}(\text{saldmen})(\text{H}_2\text{O})\text{Fe}(\text{CN})_6]$  [53]. For **13**, the  $M$  value at the maximum available field of 70 kOe is  $3.99 \mu_B$ , which is less than  $5 \mu_B$ , the value estimated for ferromagnetically paired  $\text{Mn}^{\text{III}}$  ( $S = 2$ ) and  $\text{Re}^{\text{IV}}$  ( $S = \frac{1}{2}$ ), with a  $g_{av} = 2.0$ , resulting in a magnetic field ( $H_A$ ) of approximately 120 kOe. This is less than the estimated lower limit of the saturation magnetic field ( $H_A$ ) for **12**. Unlike the chain, the dimer displays magnetic hysteresis at  $T = 1.8$  K, with a very small coercive field of 156 Oe [46].

#### AC Magnetic Measurements

The temperature-dependent compartment of the  $ac$  susceptibilities of **12** was investigated in a zero- $dc$  field. The results undoubtedly show that both the real and imaginary parts of the  $ac$  susceptibility have pronounced frequency dependence below 4 K [46]. However, not a single peak was recorded for  $\chi''(T)$  plots at the temperatures 2–4 K, as the magnetization-blocking temperature ( $T_b$ ) for **12** appears to be below 2 K [46].

For an anisotropic magnetic molecular wire, the  $\chi'T$  is proportional to the correlation length ( $\xi$ ) and obeys the formula  $\chi'T = C_{eff} \exp(\Delta\xi/k_B T)$ ,  $\Delta\xi$  being an energy necessary to produce a domain wall, and  $C_{eff}$  being the effective Curie constant per magnetic entity [10,11,54,55]. Thus, the  $ac$  susceptibility data for **12** from 2 to 11 K obtained using an  $H_{ac} = 2.7$  Oe and  $H_{dc} = 0$  Oe field and a frequency of 1 Hz were employed to analyze the SCM behavior of the compound. As expected, the  $\ln(\chi'T)$  vs.  $1/T$  plot exhibits a linear interval from 10 to 6 K, yielding  $\Delta\xi/k_B = 6.66$  K and  $C_{eff} = 1.005 \text{ emu K mol}^{-1}$  [46]. At 4.5 K,  $\ln(\chi'T)$  achieves a peak ( $(\chi'T)_{max} = 10.3 \text{ emu K mol}^{-1}$ ) and then drops linearly with temperature, reducing until  $\chi'$  is blocked. An intersection of this linear region occurring at  $\sim 4.5$  K [46] is a crossover temperature ( $T^*$ ), where the magnetic correlation is physically limited by crystal defects, and temperatures below  $T^*$  comprise the finite-sized regime [46,54].

The dynamic magnetic properties of complex **13** were studied in a frequency interval of 1–1500 Hz under an oscillating  $ac$  magnetic field of 3.5 Oe using  $H_{dc} = 100$  Oe (Figure 16) [46]. Both sets of plots indicate the presence of two relaxation processes, which may be due either to an expression of two diverse relaxation mechanisms or to the existence of a second

phase, the latter option being the most likely explanation, as a stratum of a desolvated solid could be formed on the surface of crystals of **13** [46].

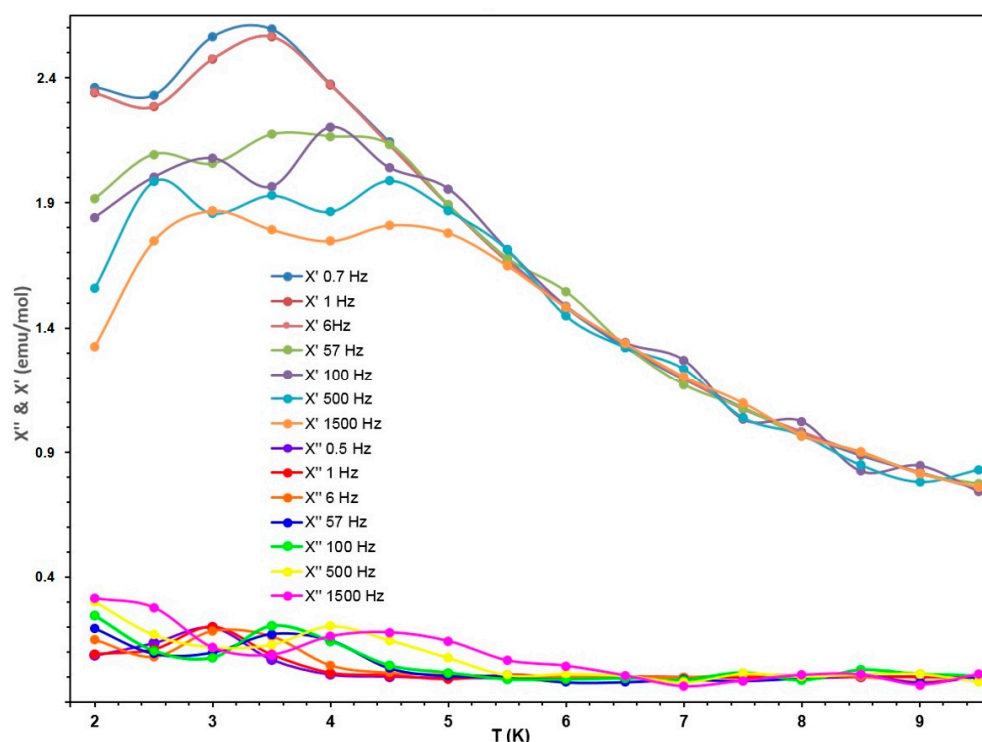


**Figure 16.** Variable-temperature real ( $\chi'$ , top) and imaginary ( $\chi''$ , bottom) *ac* molar susceptibility data for **13** under  $H_{dc} = 100$  Oe and  $H_{ac} = 3.5$  Oe. Solid lines are guides [46].

Figure 13 demonstrates that the dimers of **13** are linked in a chain by a set of hydrogen bonds. The removal of at least one  $\text{H}_2\text{O}$  molecule inevitably leads to a rearrangement of the entire packaging of binuclear entities. This results in a change in the intermolecular distances and geometric features in a dimer after the removal of all  $\text{H}_2\text{O}$  in **13**. Moreover, a reorganization in a 1D polymer is possible; the  $[\text{Mn}(\text{SB}^{2+})]^{3+}$  cations are linked to  $\text{Re}^{\text{IV}}$  ions by apical and equatorial cyanides. Such an organization of the chain in the crystal should promote a mutual alignment of both the apical axes of the  $\text{Re}(\text{CN})_7$  anions and the Jahn–Teller axes of the  $[\text{Mn}(\text{SB}^{2+})]^{3+}$  cations, which is important to increase the coercivity of LD magnets. It should be noted that the mutual slope of the  $(\text{N}\equiv\text{C}-\text{Re}-\text{C}\equiv\text{N})_{\text{apical}}$  and  $\text{N}-\text{Mn}-\text{N}$  axes (predetermined by the  $\text{Mn}-(\text{N}\equiv\text{C})$  angle) is responsible for the nature and magnitude of the intrachain coupling affecting the spin–reversal barrier height and the value of  $T_b$  [46].

#### Magnetic Measurements at Very Low Temperatures

Additional magnetization data (Figures 14 and 15) were collected from single crystals down to 30 mK. As shown in Figure 17a for **12**, the  $M/M_s(H)$  hysteresis opens only below 1.6 K. For this reason, hysteresis was not registered at 2 K for the polycrystalline sample of **12** (Figure 14), whereas for the polycrystalline sample of **13**, a tiny hysteresis loop was detected at 1.8 K [46]. The coercivity of 1.3 T is observed for a crystal of **12** at 0.4 K, which is less than the value of 1.68 T obtained for its congener  $[\text{Mn}(\text{SB}^{2+})\text{Fe}(\text{CN})_7]\cdot 4\text{H}_2\text{O}$  [20]. Considering the 1D nature of **12**, based on the  $\ln(\chi'T) - 1/T$  plot, the magnetization slow relaxation is also evident from the hysteresis loops and strongly supports the concept that **12** is a new example of a single-chain magnet with  $T_b \approx 1.6$  K [46].

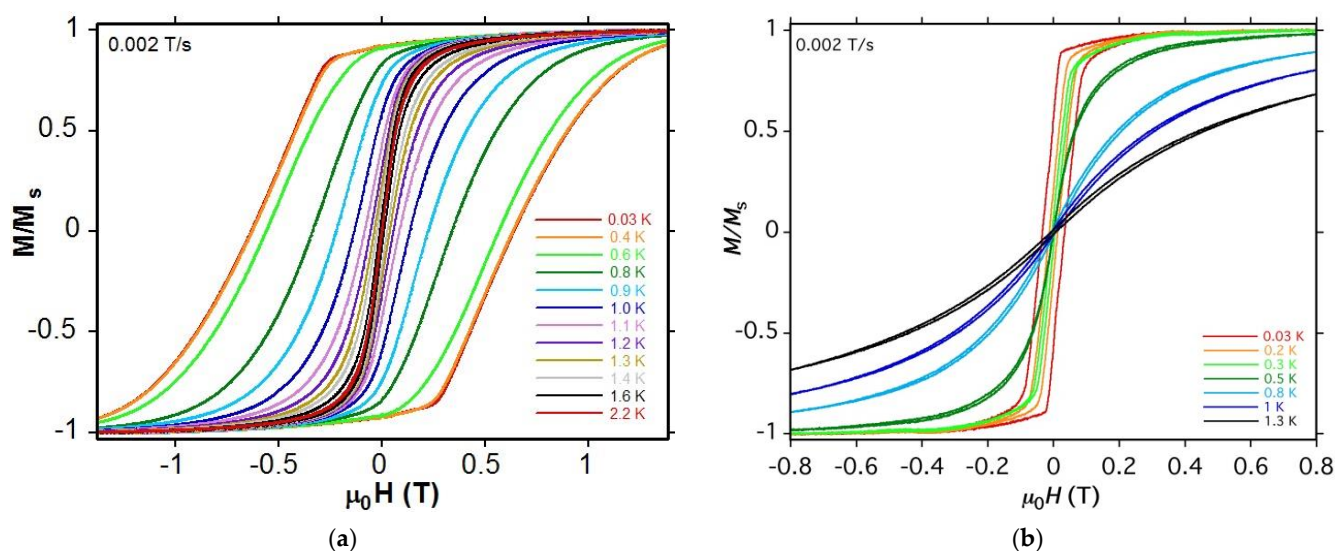


**Figure 17.** Field dependencies of the normalized magnetization measured at low temperatures from oriented single crystals with the  $H_{dc}$  applied along the easy axis: (a) for **12**; (b) for **13** [46].

Despite the presence of hysteresis, the pronounced frequency dependence of molar susceptibility, and the 0D structure, a definition of the relaxation type (SMM or SCM) of complex **13** is not straightforward. In contrast to **12**, a hysteresis loop opens at 1.8 K for a powder of **13**. Moreover, as shown by low-temperature studies (Figure 17b), the shape of the hysteresis and the coercivity of **13** are preserved for a single crystal up to 0.8 K [46]. At 0.5 K, the coercivity at  $H = 0$  collapses and, starting from  $\sim 0.4$  K, the shape of the hysteresis changes, which may also be related to the existence of the aforementioned dehydrated layer, which leads to the coexistence of two different magnetic phases with two different magnetization-blocking temperatures of  $\sim 1.8$  and  $\sim 0.4$  K—presumably for 1D and 0D phases, respectively [46]. Such an assumption is also maintained by the finding of straight sectors on the  $\ln(\chi T) - 1/T$  plot [46].

Thus, two neutral, LD heterometallic assemblies consisting of the dimer  $[\text{Mn}^{\text{III}}(\text{SB}^{2+})\text{Re}(\text{CN})_7]$  unit were obtained. As preliminary magnetic studies showed, the compound  $\{[\text{Mn}(\text{SB}^{2+})\text{Re}(\text{CN})_7](\text{H}_2\text{O})_7\}_n$  (**12**) is the only SCM based on orbitally degenerate PBP heptacyanidorhenate. The  $\chi T$  behavior of 1D and 0D compounds in a high-temperature region diverges considerably, approving the ferrimagnetic and ferromagnetic character of magnetic exchange interactions (EIs) for **12** and **13**, respectively [46]. However, at temperatures below 60 K, ferromagnetic EIs prevail in both compounds up to a temperature of 4.5 K, at which a maximum is observed in the  $\chi T - T$  plot; then,  $\chi T$  rapidly decreases due to saturation in the field effect [46]. For both compounds, even under a field of 70 kOe, the magnetization does not reach the maximum value of  $5 \mu_B$ , which is expected for five unpaired electrons, which is due to the high anisotropy of these systems, as evidenced by the estimated values of the field  $H_A$  of 151 and 120 kOe for **12** and **13**, respectively [46].

The unusual magnetic properties of both compounds originate from the interplay of Re–Mn anisotropic spin coupling and the ZFS effect of  $\text{Mn}^{\text{III}}$  ions with a noncollinear orientation of the local magnetic axes in crystals of the compounds, which was initially found for a  $\text{Mn}_3\text{Re}$  3D framework [44]. The obtained experimental data in this study could be used to theoretically model this intriguing magnetic behavior in order to determine the magnetic characteristics for anisotropic exchange, as was performed by employing microscopic theory for 3D  $[(\text{Mn}^{\text{III}}\text{acacen})_3\text{Re}^{\text{IV}}(\text{CN})_7]_n$  [44] and  $[(\text{MnL}^{\text{N5}}(\text{H}_2\text{O}))_2\text{Mo}(\text{CN})_7]$  [39].

### 3.3.3. 2D $[\text{Cat}\{(\text{Mn}(\text{acacen})_2\text{Re}^{\text{III}}(\text{CN})_7)\}_n]$ , Cat = $\text{Ph}_4\text{P}^+$ (**14**) and $\text{PPN}^+$ (**15**)

Employing tetraphenylphosphonium ( $\text{Ph}_4\text{P}^+$ ) as an additional cation led to a preparation of 1D heterometallic negatively charged polymers  $(\text{Ph}_4\text{P})_2[\text{Mn}^{\text{III}}(\text{acacen})\text{M}^{\text{III}}(\text{CN})_6]$

( $M^{III} = Fe$  or  $Os$ ) possessing SCM properties [14,21,48]. This prompted us to explore the large organic cations for the design of anionic LD molecular magnets comprising  $[Re^{IV}(CN)_7]^{3-}$  and  $[Mn^{III}(acacen)]^+$  tectons. However, when an assembling process was implemented in an alcohol mixture (MeOH, EtOH, and *li*-PrOH (1:1:1)), a 2D heterometallic complex  $Ph_4P^+[\{Mn(acacen)_2Re(CN)_7\} \cdot Solv]$  (**14**) was obtained for the first time. However, the replacement of  $Ph_4P^+$  by bulkier  $PPN^+$  did not result in the formation of an anionic chain. However, in this case, a layered material,  $PPN^+[\{Mn(acacen)_2Re(CN)_7\} \cdot Solv]$  (**15**), was also formed, with a 2D coordination network possessing unique magnetic properties [56].

### Crystal Structure Descriptions

In spite of the fact that single crystals were grown for layered compounds, a structure with a satisfactory R factor was solved only for the  $PPN^+$  derivative **15**. The independent part of a layer in **15** and a cation  $PPN^+$  are shown in Figure 18. Figure 19 demonstrates a two-dimensional network structure consisting of two sets of crossed chains; in one, the  $[Re(CN)_7]^{3-}$  metalloligand binds the neighboring  $[Mn(acacen)_2]^+$  moieties (see Scheme 2) by its apical axis, and the other does so with two equatorial CN ligands [56]. The hybrid layered packing of **15** consists of the anionic coordination networks separated by a space containing individual organic cations. It can be plainly observed by projecting the structure onto the *ac* or *bc* plane. The distances between the Re centers located in the nodes of the 2D network correspond to the values of the crystal cell parameters *a* and *b* ( $a = b = 10.9343(2)$  Å), which are close to those of the neutral material,  $[Mn(acacen)_2[Ru(CN)_5NO]$  [41]. The distance between the planes of adjacent layers matches parameter *c* of the 2D network [56]. The 2D polymer **15** is the least symmetrical coordination network among the known earlier layered assemblies involving cyanide metalloligands  $[K(18-cr)(2-PrOH)_2][Mn(acacen)_2][Fe(CN)_6]$  [57] and  $K[Mn(acacen)_2][W(CN)_8] \cdot 2H_2O$  [58].

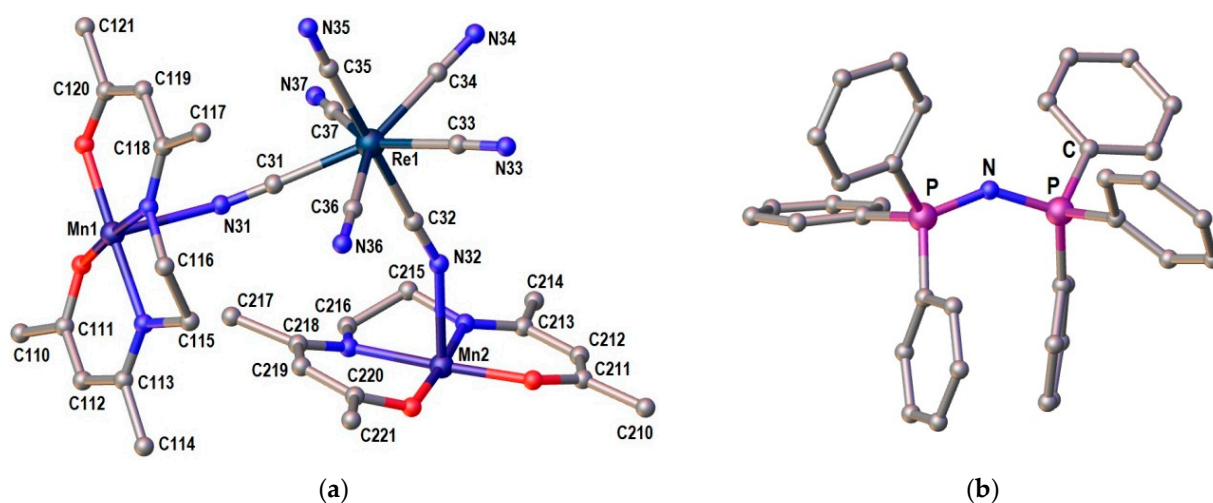


**Figure 18.** (a) Independent part,  $[\{Mn(acacen)_2Re(CN)_7\}^-]$ , of **15** with the atom-numbering scheme of unique atoms; (b)  $PPN^+$  molecular structure. Triclinic,  $P1$ ; *a*, *b*, *c* (Å): 10.7016(5), 10.8268(5), 16.2004(7);  $\alpha$ ,  $\beta$ ,  $\gamma$  ( $^\circ$ ): 102.662(1), 93.607(1), 90.207(1);  $V = 1827.47(14)$  (Å<sup>3</sup>),  $Z = 1$ ,  $T = 298$  K [56].

Each  $[Re^{IV}(CN)_7]^{3-}$  metalloligand is linked to four  $[Mn(acacen)]^+$  cations by means of four cyanides with corresponding distances:  $Mn1-N31_{apical}$  of 2.384(3) Å and  $Mn2-N32_{equat}$  of 2.299(5) Å. The  $Mn-N \equiv C$  bond angles are 154.5(5) and 155.2(3) $^\circ$  for apical and equatorial cyanide respectively, indicating that the bridging CN ligands coordinate to  $Mn^{III}$  ions in a bent mode [56], although this bending is substantially less than the 144.2 $^\circ$  and 145.1 $^\circ$  observed in **12** and **13**, respectively.

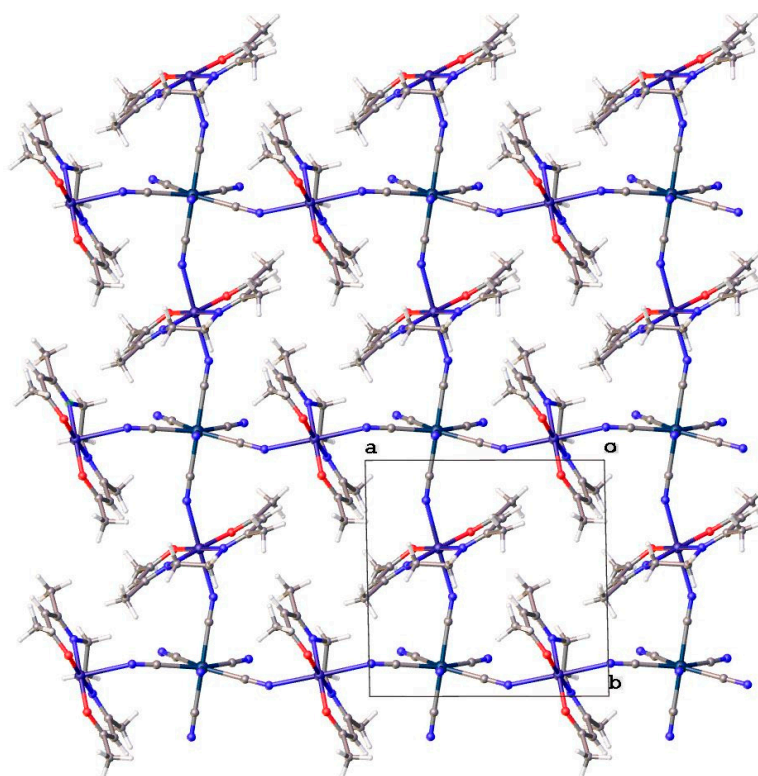


**Figure 19.** Projection of the anionic layer along the  $c$  axis of **15**, showing a two-dimensional network structure consisting of two types of crossed chains [56].

The Re polyhedron is sufficiently close to an ideal PBP because the Re—C bond length changes in the range of 2.090(5)—2.115(3) Å, with the C—Re—C angles only slightly differing from the ideal geometry. The Mn environment is an elongated octahedron characteristic of the high-spin  $\text{Mn}^{\text{III}} d^4$  electronic configuration. This is due to the Jahn–Teller effect of the combination with a strong in-plane donation of the  $\text{acacen}^{2-}$  ligand [56]. The in-plane Mn—ligand bond distances fall in the 1.898(4)—1.988(6) Å range, whereas the axial Mn—N bond distances are elongated: Mn1—N31 = 2.384(3), Mn1—N34 = 2.321(3) Å, Mn2—N32 = 2.299(5), and Mn2—N35 = 2.279(5) Å. Such a situation is typical for hetero-bimetallic materials, including  $\text{Mn}^{\text{III}}(\text{SB})$  complexes and polycyanide metalloligands [9,57].

The space between the anionic layers is occupied by  $\text{PPN}^+$  cations and highly disordered solvent molecules. When deposited in CCDC, the latter were refined as water molecules; however, in accordance with the result of elemental analysis, they were approximately defined as a mixture of water and ethanol in order to establish a system of hydrogen bonds. In particular, it should be noted that the crystals of **15** are able to lose part of the solvent, retaining their integrity [56].

Although several batches of the crystals of **14** were verified, their structure was resolved only partially. An SCXRD investigation for **14** was conducted at 298 K, yielding the following cell parameters for **14**:  $a = b = 15.1259(15)$ ,  $c = 61.625(7)$  Å,  $\beta = 90^\circ$ ,  $V = 14,105(3)$  Å<sup>3</sup>,  $Z = 8$ —much higher than those of **15**. Notwithstanding that, a layered organization was also defined for **14** with four layers per cell located perpendicular to the  $c$  axis (Figure 20) [56].

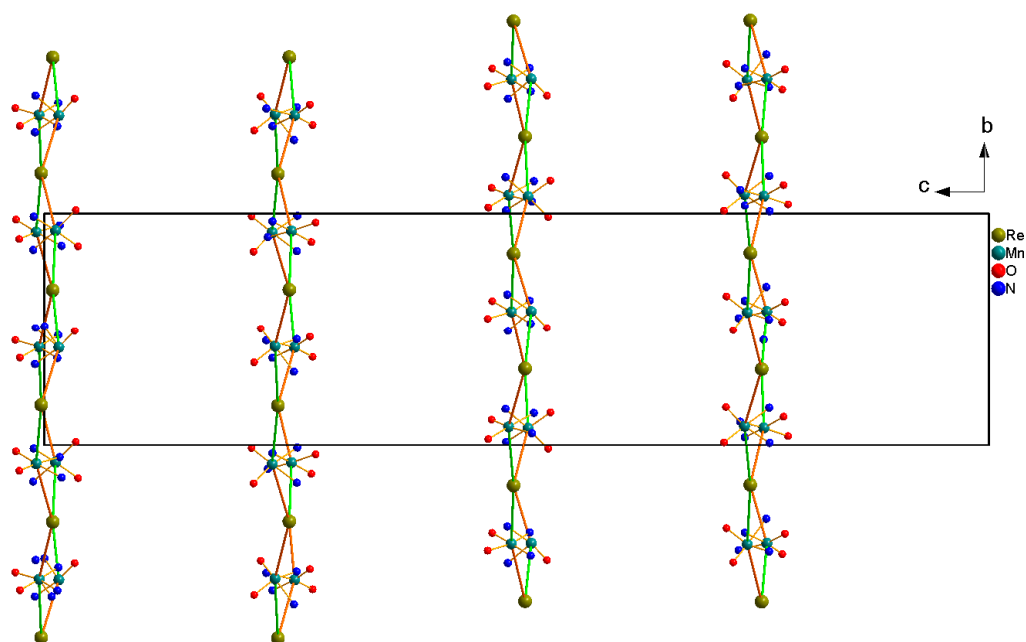


**Figure 20.** A view of four layers in **14** along the  $a$  axis. The  $\text{Re-CN}_{\text{apical}}\text{—}\{\text{MnN}_2\text{O}_2\}$  and  $\text{Re-CN}_{\text{equatorial}}\text{—}\{\text{MnN}_2\text{O}_2\}$  connections are colored in green and orange, respectively [56].

The space group was chosen based on the distribution of heavy atoms. In addition, it was able to localize most of the atoms from the nearest environment of Re and Mn. This was sufficient to establish inner-layer organization. In the 2D network of **15**, there are two types of perpendicular chains, in one of which the Mn ions are connected by two apical cyanides of the metalloligand, and in the other, by equatorial CN-groups, whereas in the 2D material **14**, the layers are more “corrugated” (see Figure 21) because their mutually perpendicular chains are organized equally; the Mn centers are connected to the Re ions both by apical and equatorial cyanides. This is manifested in the distances between metal centers. If in a layer of **15**, there are only two types of distances between Mn atoms, i.e., 10.8268(5) and 1.7016(5) Å (for apical and equatorial cyanides, respectively), then in the layers of **14**, there are as many as four possible distances of Mn—Mn for each layer (for the middle layer, the “apical” and “equatorial” distances are 10.7825(8) and 10.7612(8) Å, 10.6374(5) and 10.6173(5) Å respectively). These structural features are extremely important for understanding the difference in magnetic behavior between **14** and **15** [56].

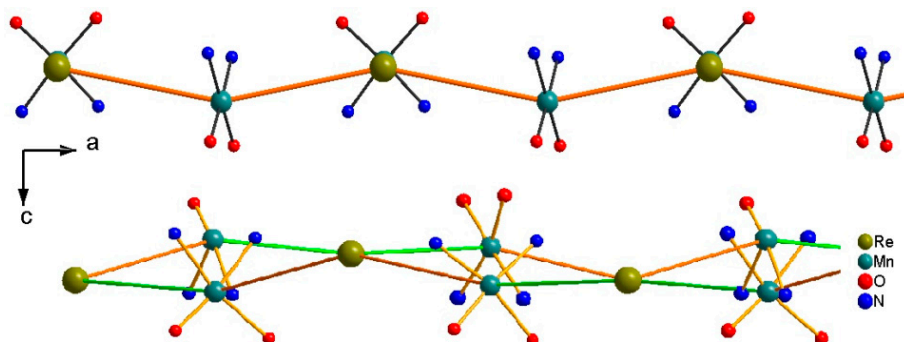


**Figure 21.** Schematic presentation of the anionic layer of **15** (top) and **14** (bottom), with projection along the  $b$  axis. The  $\text{Re-CN}_{\text{apical}}\text{—}\{\text{MnN}_2\text{O}_2\}$  and  $\text{Re-CN}_{\text{equatorial}}\text{—}\{\text{MnN}_2\text{O}_2\}$  connections are colored in green and orange, respectively [56].

### Static Magnetic Studies

The temperature dependencies of the *dc* molar susceptibility for the powder samples of **14** and **15** are presented in Figure 22 as  $\chi T$  vs.  $T$  plots. At 300 K, the  $\chi T$  values of 6.55 and 6.50 emu K mol<sup>-1</sup> (for **14** and **15**, respectively) are close to the 6.51 emu K mol<sup>-1</sup> expected for two Mn<sup>III</sup> ( $S = 2$ ,  $g = 2.03$ ) [44] and one Re<sup>IV</sup> ( $S = 1/2$ ,  $g = 2.33$ ) [38] nonintersected spins [56]. As can be seen in the inset of Figure 22, showing the zoomed-in plots in the  $\chi T$  range from 4 to 11 emu K mol<sup>-1</sup>, the magnetic behavior of the two networks is similar [56]. This is particularly true at high temperatures. Starting from 300 K, the  $\chi T$  curves decrease slightly and then reach a light minimum of 5.94 emu K mol<sup>-1</sup> at ~85 K for **15** and 5.57 emu K mol<sup>-1</sup> at ~35 K for **14** [56]. With a further decrease in temperature, the  $\chi T$  plots increase and reach maximums of 10.51 emu·K·mol<sup>-1</sup> at ~11.5 K for **14** and 181.45 emu·K·mol<sup>-1</sup> at 18 K for **15** before dropping to 7.75 and 27.54 emu K mol<sup>-1</sup> at 2 K for **14** and **15**, respectively [56]. Such compartment of  $\chi T$  is characteristic of the ferrimagnetic interaction between the metal ions inside the chains [44,52].

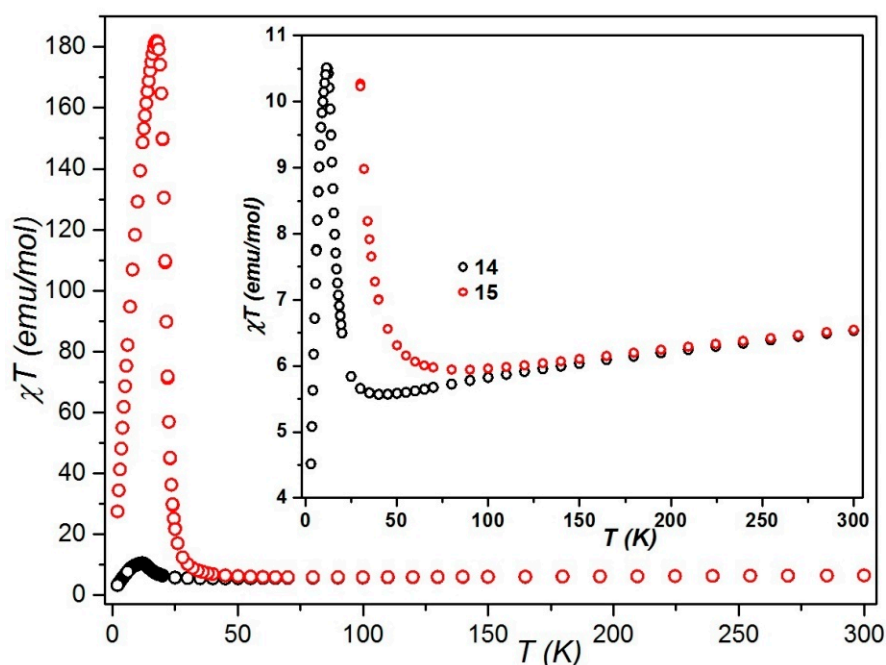


**Figure 22.** Magnetic *dc* plots for **14** and **15**. Temperature dependencies of  $\chi T$  at  $H = 1000$  Oe. Inset: zoomed-in magnetization versus field at  $T = 2$  K [56].

In Figure 23, the magnetization data for both the layered materials are presented. The high-field magnitude of  $3.62 \mu_B$  M for **14** is close to the  $3.58 \mu_B$  registered for the chain  $\{[\text{Mn}^{\text{III}}(\text{SB}^{2+})\text{Re}^{\text{IV}}(\text{CN})_7]\}_n$  (**12**) [46]. The initial magnetization plot for **15** displays an S shape typical for metamagnetic materials. In the field of 23205, a metamagnetic transition takes place at 2 K [56]. The  $M$  value of  $3.2 \mu_B$  at the maximum available field of 7 T is very far even from the  $7 \mu_B$  calculated for antiferromagnetically coupled Mn<sup>III</sup> ( $S = 2$ ) and Re<sup>IV</sup> ( $S = 1/2$ ) with  $g_{av} = 2.0$ . The limit of the anisotropic magnetic field ( $H_A$ ) for **15** estimated by linear approximation is 26 T [56], which is considerably larger than an estimation of 15 T obtained for **12**. Studies of initial  $M(H)$  plots for **15** at different temperatures (Figure 24) show that the S shape of the curve disappears at temperatures above 5 K [56]. Such behavior of  $M$  below 5 K is reminiscent of a metamagnetic transition from an antiferromagnetic state to a polarized state, as found for the related 3D framework material **11** [44].

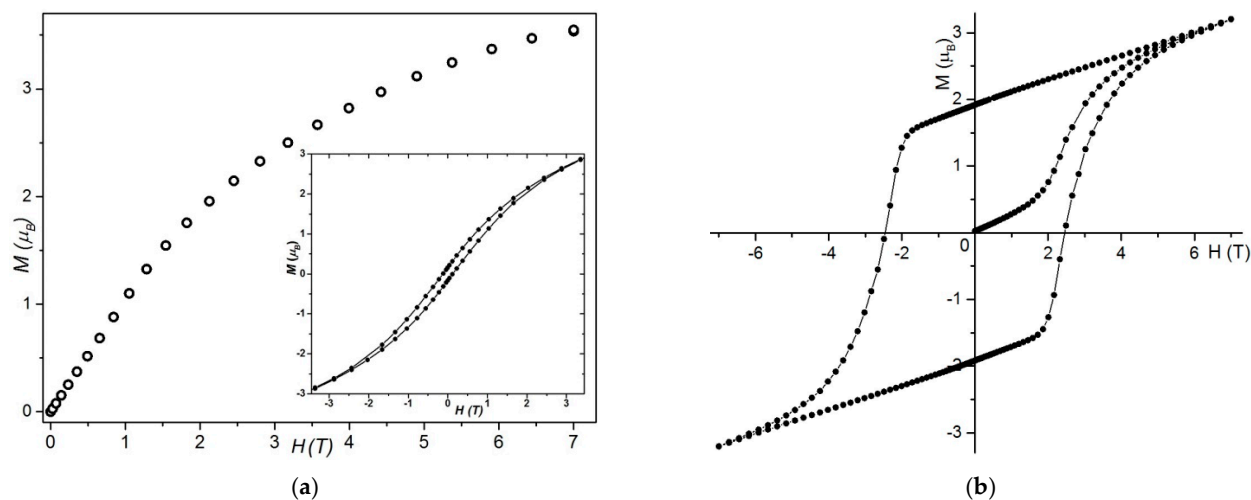


**Figure 23.** Magnetization plots at 1.8 K and a field sweep rate of 700 Oe/s. (a) Initial magnetization vs. the field plot and magnetic hysteresis (inset) for 14. (b) Initial magnetization vs. the field plot and magnetic hysteresis for 15 [56].

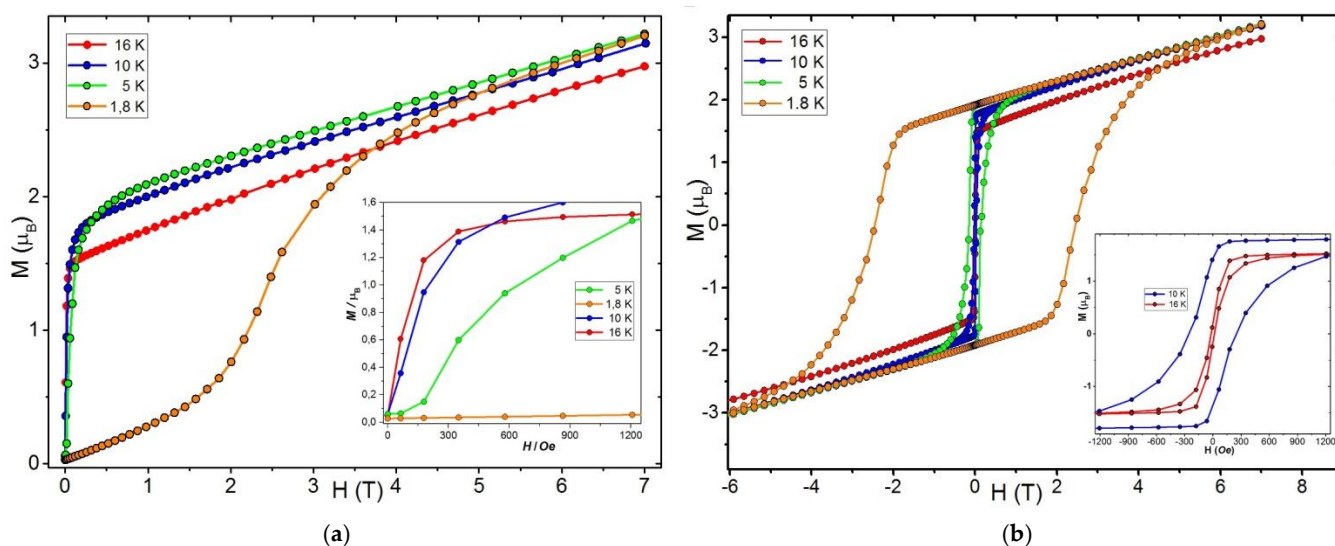


**Figure 24.** Magnetization plots for 15 measured on a polycrystalline sample at various temperatures and a field sweep rate of 700 Oe/s. (a) Initial magnetization plots. (b) Magnetic hysteresis loops. Inset the zoomed-in low-field region for the data collected at 10 and 16 K [56].

As can be seen in Figure 23, both 2D polymers exhibit magnetic hysteresis at  $\sim 2$  K, with compound 14 showing a hysteresis with a small coercive field of 1150 Oe, whereas for 15, this parameter reaches a value of 2.486 T, which is much larger than that of 1.5 T observed for an oriented single crystal of SCM,  $[\text{Mn}^{\text{II}}(\text{bida})(\text{H}_2\text{O})]_2[\text{Mo}^{\text{III}}(\text{CN})_7] \cdot 6\text{H}_2\text{O}$  [17]. The  $M(H)$  of 15 does not saturate in the field of 7 T (70 kOe) and reveals a linear dependence at high fields, which is typical for strongly anisotropic systems [56]. The hysteresis plots of 15 measured at higher temperatures are presented in Figure 24a, with the inset of this figure demonstrating that a very tiny hysteresis loop is still visible at 16 K, which indicates that the critical temperature for this 2D material is only slightly higher than 16 K [56].

#### Dynamic Magnetic Studies

The *ac* data of the  $[\text{Mn}^{\text{III}}(\text{acacen})\text{Re}^{\text{IV}}(\text{CN})_7]^{2-}$  networks were also collected as the temperature- and frequency-dependent susceptibilities. The study results are shown in Figure 25. The temperature dependencies for different frequencies of  $\chi'$  and  $\chi''$  susceptibil-

ity data for **14** and **15** were determined in  $H_{dc} = 100$  Oe and  $H_{ac} = 3$  Oe. Both  $ac$  components of **14** are frequency-dependent, and the  $\chi'$  susceptibility of **14** displays two apparent relaxation processes, whereas no second relaxation process was found for  $\chi''$  [56].

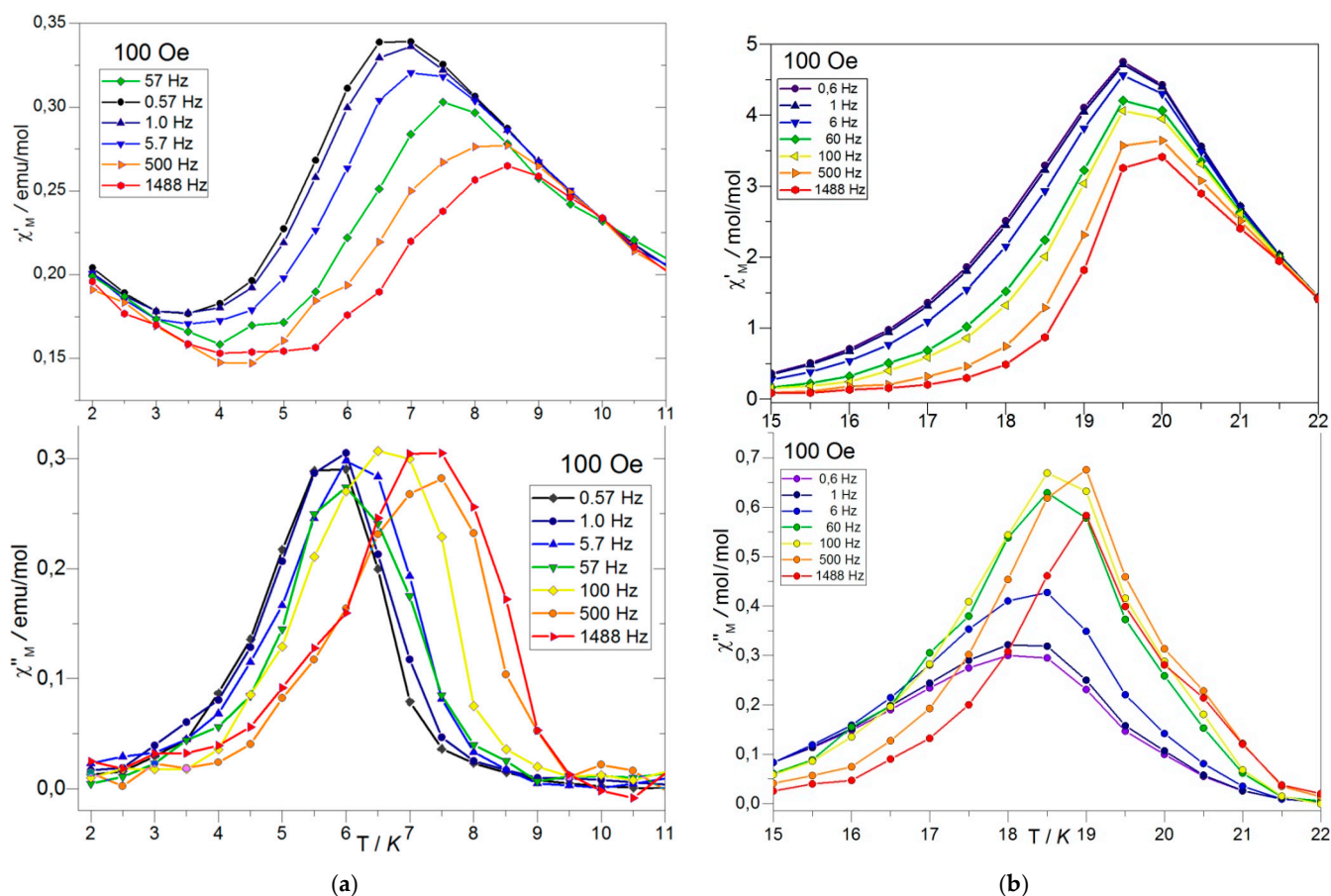


**Figure 25.** Variable temperature of the real ( $\chi'$ , top) and imaginary ( $\chi''$ , bottom) parts of the  $ac$  molar susceptibility data collected under  $H_{dc} = 100$  Oe and  $H_{ac} = 3$  Oe. Solid lines are guides for (a) **14** and (b) **15** [56].

The lack of points for the  $ac$  data for **15** (Figure 25b) prevents determination of the positions of the peaks for both, as well as parts of the  $ac$  susceptibility. It seems that for  $\chi'$ , the effect of the frequency results only in a reduction in the peak intensity, without affecting the position of the peaks at  $\sim 19.75$  K. However, for  $\chi''$ , in addition to increasing the intensity of the peak, the peaks shift to slightly higher temperatures.

An SCM behavior test was also carried out for **14** and **15** by means of the  $\ln(\chi'T) - 1/T$  plot. Figure 26 shows the  $\ln(\chi'T) - 1/T$  plots for **14** and **15**. Linear regions are presented for both compounds. For **14**, the temperature range of 11–8.5 K results in  $C_{eff} = 0.48$  emu K mol $^{-1}$  and  $\Delta\zeta/k_B = 3.62$  K, with  $\ln(\chi'T)$  reaching a maximum at 8 K and then experiencing a straight decrease with reduced temperature until  $\chi'$  blocking. An intersection of the two linear intervals at  $\sim 7.1$  K corresponds to a crossover temperature ( $T^*$ ) [54,55]. Hence, it can be assumed that the dependence of  $\chi'$  on frequency is due to slow magnetic relaxation of the chains, of which the 2D network of **14** is composed [56].

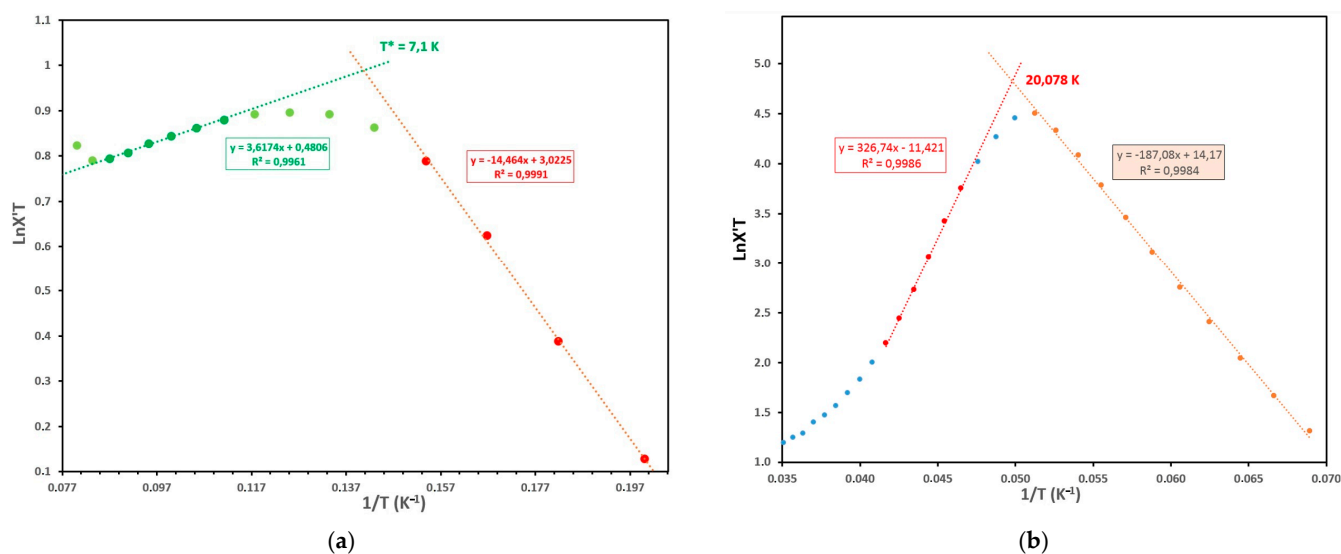


**Figure 26.** Plots of  $\ln(\chi'T)$  vs.  $1/T$ , where  $\chi'$  is a real component of the  $ac$  susceptibility collected in the applied  $dc$  field of 100 Oe, with  $H_{ac} = 3$  Oe, and a frequency of 0.56 Hz; (a) for **14**; (b) for **13** [56].

An analogous procedure performed for **15** as presented in Figure 26b showed that in a linear region in the range of 24–21.5 K with  $\Delta\bar{\xi}/k_B = 326.74$  and  $C_{eff} = 11.42$  emu K mol<sup>-1</sup>, the crossover temperature,  $T^* = 20.1$  K, was somewhat higher than the  $T_B$  of ~16 K based on magnetization measurements for **15** but very close to the value of 19.75 K based on  $\chi'$  data (Figure 25b). Unlike the 2D networks of  $[\text{Mn}^{\text{III}}(\text{acacen})\text{Re}^{\text{IV}}(\text{CN})_7]^{2-}$  studied in ref. [56], the frequency dependence of the  $ac$  data was not found for 3D framework **11** [44], the nearest relative. For the latter, nevertheless, a phase transition was also found at 13 K, which is ~7 K lower than for **15**.

The presented combined  $dc$  and  $ac$  magnetic data, as well as the positive testing for SCM behavior of both networks, may testify to the existence of magnetic relaxation in the chains of which the anionic layers of coordination polymers **14** and **15** are composed. As follows from the SCRD data, the layers are well-insulated from each other by organic cations, which preclude the realization of a pseudo-3D structure, resulting in long-range 3D order characteristic of conventional magnets [56]. Thus, the magnetic hysteresis recorded for these two materials is scarcely a result of a phase transition, owing to the presence of mutually perpendicular 1D polymers composed of anisotropically coupled spin carriers [56]. This is confirmed by a noteworthy dissimilarity in magnetic behavior of **14** and **15**, as there is an essential difference in the structure of the -Re-Mn-Re-Mn- chains for these materials [56]. The lower  $T_B$  for **14** is due to the alternating binding of Mn ions in the parallel chains by the metalloligand  $[\text{Re}(\text{CN})_7]^{3-}$ , which combines two kinds connections: through apically located cyanides and equatorial cyanides in the same chain. Moreover, such an alternation is observed for both types of perpendicularly located chains in a layer. Whereas in **15**, these chains differ significantly in the manner of binding—apical in one type of parallel chains and equatorial in the chains perpendicular to the first. This combination considerably increases the magnetic anisotropy of the  $\text{Re}^{\text{IV}}-\text{Mn}^{\text{III}}$  heterobimetallic system, emphasizing a direction along the crystal axis ( $b$ ) as the direction of easy magnetization [56]. In contrast, the orientation along the  $a$  axis results in less magnetization, and the orientation along the  $c$  axis corresponds to the hard magnetization axis [56].

Of particular note is the coercive field of 2.486 T for **15**, which is a record for heterobimetallic molecular magnets based on homoleptic polycyanide metalloligands. The unusual magnetic properties of both compounds originate from the interplay of Re–Mn anisotropic spin coupling and the ZFS effect of  $\text{Mn}^{\text{III}}$  ions with a noncollinear orientation of the local magnetic axes in crystals of the compounds [56].

### 3.3.4. Heterobimetallic Assemblies of $[\text{Re}^{\text{IV}}(\text{CN})_7]^{3-}$ with Some Monocationic Complexes $[\text{Mn}^{\text{III}}(\text{SB})]^+$ of Salen-Type Schiff Bases

Here, we briefly describe the compounds obtained on the basis of two salen-based  $\text{Mn}^{\text{III}}$  complexes, as their magnetic properties have not been studied. However, they deserve mentioned in this review, as there are not many heterometallic assemblies containing such *salen* complexes of  $\text{Mn}^{\text{III}}$  in their composition. We would like to draw the reader's attention on the four heterometallic complexes, which were relatively recently synthesized, studied, and structurally characterized [59].

Two compounds were used as precursors—one was a previously known mononuclear complex,  $[(\text{Mn}^{(3\text{MeO})\text{Salen}})_2(\text{H}_2\text{O})_2](\text{ClO}_4)_2 \cdot 2\text{H}_2\text{O}$  (**16**) [60], and the other was a binuclear complex,  $[\text{Mn}_2^{(5\text{Me})\text{Salen}}\text{OAc}]\text{PF}_6$  (**17**), which was obtained by us. In the case of **16**, a slow diffusion of the component solutions led to the ionic compound  $\text{Ph}_4\text{P}[\text{Mn}^{(3\text{MeO})\text{Salen}}(\text{H}_2\text{O})_2]_2[\text{Re}(\text{CN})_7] \cdot 6\text{H}_2\text{O}$  (**18**) [59]. The direct mixing of the same solutions resulted in a microcrystalline and nearly insoluble solid,  $[\text{Mn}^{(3\text{MeO})\text{Salen}}(\text{H}_2\text{O})]_4\text{Re}(\text{CN})_7\text{ClO}_4 \cdot 1.5\text{MeCN} \cdot 6.5\text{H}_2\text{O}$ , which is likely to comprise the pentanuclear clusters  $[(\text{Mn}^{\text{III}}(\text{SB})(\text{H}_2\text{O}))_4\text{Re}(\text{CN})_7]^+$  [59]. The employment of **16** resulted in a 2D network assembly of octanuclear clusters,  $[(\text{Mn}^{(5\text{Me})\text{Salen}})_6(\text{H}_2\text{O})_2\text{Re}(\text{CN})_7]_2\text{Re}(\text{CN})_7\text{Cl}_2(\text{PF}_6) \cdot \text{H}_2\text{O}$  (**19**), incorporating two Re centers in a PBP coordination environment, whereas another had a strongly distorted capped trigonal prism as a coordination polyhedron [59]. The latter was observed for the first time for  $\text{Re}(\text{IV})$  complexes [59]. A synthetic challenge to obtain the 0D assemblies with a ratio of  $\text{Re}:\text{Mn} \geq 3$  yielded a hexanuclear compound,  $[\text{Mn}^{(5\text{Me})\text{Salen}}\text{H}_2\text{O}(i\text{-PrOH})][(\text{Mn}^{(5\text{Me})\text{Salen}})_5\text{H}_2\text{O}(i\text{-PrOH})_2\text{Re}(\text{CN})_7](\text{PF}_6)_2(\text{OAc}) \cdot 2i\text{-PrOH}$  (**19**), which is a 1D polymer formed by a bridging phenoxyl group [59].

## 4. Conclusions

The recently studied 1D and 2D heterometallic  $\text{Mn}^{\text{III}}\text{--Re}^{\text{IV}}$  compounds have made the  $[\text{Re}^{\text{IV}}(\text{CN})_7]^{3-}$  family more representative in terms of the dimensionality of the known assemblies. All magnetically characterized family members have a strong anisotropy, which is determined by complexly organized anisotropic exchange interactions caused by the unquenched orbital momentum of  $\text{Re}^{\text{IV}}$  and local ZFC of  $\text{Mn}^{\text{III}}$  ions, as well as by the mutual arrangement of the apical axes, i.e., the Jahn–Teller axes for Mn and the  $D_{5h}$  axes of the Re PBP.

Two 2D heterobimetallic networks based on orbitally degenerate heptacyanidorhenate(IV) were synthesized for the first time and magnetically studied. An analysis of the magnetic data sets for the polycrystalline samples of  $\text{Ph}_4\text{P}[\{\text{Mn}(\text{acacen})\}_2\text{Re}(\text{CN})_7] \cdot \text{Solv}$  (**14**) and  $\text{PPN}[\{\text{Mn}(\text{acacen})\}_2\text{Re}(\text{CN})_7] \cdot \text{Solv}$  (**15**) showed that both materials display slow relaxation of magnetization at temperatures: below 10 and 21 K for **14** and **15**, respectively [56]. Regardless of the same molecular units that make up the networks, the studied anionic layers are quite different in terms of magnetic anisotropy, as they possess a magnetic hysteresis at 2 K: small (0.23 T) for **14** and large (~5 T) for **15**. Furthermore, for these polymers, the  $M(H)$  value does not saturate at the maximum available field of 7 T, and the network **15** is a metamagnet. This intriguing difference originates from the interplay of Re–Mn anisotropic spin coupling and the ZFS effect of  $\text{Mn}^{\text{III}}$  ions with a noncollinear orientation of the local magnetic axes in crystals of the compounds [56]. The most well-known anisotropic is the  $\text{PPN}[\{\text{Mn}^{\text{III}}(\text{acacen})\}_2\text{Re}^{\text{IV}}(\text{CN})_7] \cdot \text{Solv}$  2D network, which possesses a critical temperature of 20 K and magnetic hysteresis with a record for cyanide-bound molecular material coercivity. The factors presented above makes it very difficult to theoretically model the magnetic behavior of such systems. In fact, only the group of Prof. V. Mironov has proposed an adequate approach to this problem, using the ligand field microscopic theory.

In our opinion, there are several possible directions for the development of research on the  $\text{Re}^{\text{IV}}\text{—CN—Mn}^{\text{III}}$  system, including an improvement of synthetic approaches for the reliable preparation of both neutral and negatively charged LD assemblies. Despite the advantages of  $[\text{Re}^{\text{IV}}(\text{CN})_7]^{3-}$  as a magnetic unit, the main obstacle to the rational design of LD nanomagnets is the polydentate nature of this metalloligand. As shown in this

review, this nature leads to the formation of 2D and 3D polymers due to the participation of equatorially located cyano groups in the coordination. Although this can be avoided by using sterically hindered tricationic complexes based on  $[\text{Mn}(\text{SB}^{2+})]^{3+}$ , for the latter, the range of metal ions can be expanded by using  $\text{Fe}^{3+}$  and  $\text{Cr}^{3+}$  ions. The latter, acting as high-spin blocks and being magnetically isotropic, will not only provide more predictable magnetic behavior of target magnetic materials but also simplify its theoretical modeling. In the longer term, we are planning to develop a synthetic approach to the synthesis of doubly connected SCMs, such as  $\{[\text{M}(\text{bida})(\text{H}_2\text{O})]_2[\text{Mo}(\text{CN})_7] \cdot 6\text{H}_2\text{O}\}_n$  [17].

The most promising direction in the chemical engineering of new highly anisotropic LD assemblies with slow magnetic relaxation at high temperatures is the synthesis of orbitally degenerate PBP  $\text{Re}^{\text{IV}}$  complexes with pentadentate planar organic macrocycles, which simultaneously set the  $D_{5h}$  symmetry of the target complex and block the equatorial positions of PBP. Recently, this was achieved for the  $(\text{Et}_4\text{N})[\text{Mo}^{\text{III}}(\text{DAPBH})\text{Cl}_2]$  [61] electronic analogue  $[\text{Re}^{\text{IV}}(\text{CN})_7]^{3-}$ , but no heterometallic compounds based on it have been published to date.

Equally important is the development of theoretical modeling of the magnetic behavior for molecular magnets based on heterometallic assemblies of orbitally degenerate PBP complexes of  $d$  elements, which are the source of anisotropic exchange interactions. In order to develop theoretical methods for modeling magnetic properties of such complicated objects, it is necessary to obtain direct experimental data for their magnetic parameters, i.e.,  $D$  and tensor quantities  $J$  and  $g$ . The accomplishment of this task is possible only with the use of high frequencies and high-magnetic-field spectroscopic methods. The set of theoretical parameters thus obtained will be used in the future for practical recommendations for the rational design of high-performance SMMs.

**Funding:** This research was funded by the Ministry of Science and Higher Education of the Russian Federation (No. 121031700321-3).

**Institutional Review Board Statement:** Not applicable.

**Informed Consent Statement:** Not applicable.

**Data Availability Statement:** Not applicable.

**Conflicts of Interest:** The author declares no conflict of interest.

## Abbreviations

SMM—single-molecule magnet; SCM—single-chain magnet; PBP—pentagonal bipyramid(al); MCP—monocapped prism; LD—low-dimensional; ZFS—zero field splitting; SOC—spin-orbit coupling; SB—Schiff base; SCXRD—single-crystal X-ray diffraction; JTA—Jahn-Teller axe;  $\text{PPN}^+$ —bis(triphenylphosphine)iminium; EIs—exchange interactions.

## References

1. Mironov, V.S.; Chibotaru, L.F.; Ceulemans, A. Mechanism of a Strongly Anisotropic  $\text{Mo}^{\text{III}}-\text{CN}-\text{Mn}^{\text{II}}$  Spin-Spin Coupling in Molecular Magnets Based on the  $[\text{Mo}(\text{CN})_7]^{4-}$  Heptacyanometalate: A New Strategy for Single-Molecule Magnets with High Blocking Temperatures. *J. Am. Chem. Soc.* **2003**, *125*, 9750–9760. [[CrossRef](#)] [[PubMed](#)]
2. Mironov, V.S. New Approaches to the Problem of High-Temperature Single-Molecule Magnets. *Dokl. Phys. Chem.* **2006**, *408*, 130–136. [[CrossRef](#)]
3. Freedman, D.E.; Jenkins, D.M.; Iavarone, A.T.; Long, J.R. A Redox-Switchable Single-Molecule Magnet Incorporating  $[\text{Re}(\text{CN})_7]^{3-}$ . *J. Am. Chem. Soc.* **2008**, *130*, 2884–2885. [[CrossRef](#)] [[PubMed](#)]
4. Zadrozny, J.M.; Freedman, D.E.; Jenkins, D.M.; Harris, T.D.; Iavarone, A.T.; Mathonière, C.; Clérac, R.; Long, J.R. Slow Magnetic Relaxation and Charge-Transfer in Cyano-Bridged Coordination Clusters Incorporating  $[\text{Re}(\text{CN})_7]^{3-/4-}$ . *Inorg. Chem.* **2010**, *49*, 8886–8896. [[CrossRef](#)] [[PubMed](#)]
5. Wang, X.-Y.; Avendaño, C.; Dunbar, K.R. Molecular Magnetic Materials Based on 4d and 5d Transition Metals. *Chem. Soc. Rev.* **2011**, *40*, 3213. [[CrossRef](#)]
6. Qian, K.; Huang, X.-C.; Zhou, C.; You, X.-Z.; Wang, X.-Y.; Dunbar, K.R. A Single-Molecule Magnet Based on Heptacyanomolybdate with the Highest Energy Barrier for a Cyanide Compound. *J. Am. Chem. Soc.* **2013**, *135*, 13302–13305. [[CrossRef](#)]

7. Wang, Q.-L.; Southerland, H.; Li, J.-R.; Prosvirin, A.V.; Zhao, H.; Dunbar, K.R. Crystal-to-Crystal Transformation of Magnets Based on Heptacyanomolybdate (III) Involving Dramatic Changes in Coordination Mode and Ordering Temperature. *Angew. Chem. Int. Ed.* **2012**, *51*, 9321. [[CrossRef](#)]
8. Shi, L.; Wei, X.; Wang, X.; Wu, D. Research Progress in Molecular Magnetic Materials Based on the  $[\text{Mo}(\text{CN})_7]^{4-}$  Unit. *Sci. Sin. Chim.* **2020**, *50*, 1637–1653. [[CrossRef](#)]
9. Miyasaka, H.; Saitoh, A.; Abe, S. Magnetic Assemblies Based on Mn(III) Salen Analogues. *Coord. Chem. Rev.* **2007**, *251*, 2622–2664. [[CrossRef](#)]
10. Coulon, C.; Miyasaka, H.; Clérac, R. Single-Chain Magnets: Theoretical Approach and Experimental Systems BT. In *Single-Molecule Magnets and Related Phenomena*; Winpenny, R., Ed.; Springer: Berlin/Heidelberg, Germany, 2006; pp. 163–206, ISBN 978-3-540-33240-4.
11. Sun, H.-L.; Wang, Z.-M.; Gao, S. Strategies towards Single-Chain Magnets. *Coord. Chem. Rev.* **2010**, *254*, 1081–1100. [[CrossRef](#)]
12. Bar, A.K.; Pichon, C.; Sutter, J.-P. Magnetic Anisotropy in Two- to Eight-Coordinated Transition-Metal Complexes: Recent Developments in Molecular Magnetism. *Coord. Chem. Rev.* **2016**, *308*, 346–380. [[CrossRef](#)]
13. Coulon, C.; Pianet, V.; Urdampilleta, M.; Clérac, R. Single-Chain Magnets and Related Systems BT. In *Molecular Nanomagnets and Related Phenomena*; Gao, S., Ed.; Springer: Berlin/Heidelberg, Germany, 2014; pp. 143–184, ISBN 978-3-662-45723-8.
14. Peresypkina, E.V.; Majcher, A.M.; Rams, M.; Vostrikova, K.E. A Single Chain Magnet Involving Hexacyanoosmate. *Chem. Commun.* **2014**, *50*, 7150–7153. [[CrossRef](#)] [[PubMed](#)]
15. Majcher, A.M.; Pilet, G.; Mironov, V.S.; Vostrikova, K.E. Neutral Low-Dimensional Assemblies of a Mn(III) Schiff Base Complex and Octacyanotungstate(V): Synthesis, Characterization, and Magnetic Properties. *Magnetochemistry* **2017**, *3*, 16. [[CrossRef](#)]
16. Pedersen, K.S.; Bendix, J.; Clérac, R. Single-molecule magnet engineering: Building-block approaches. *Chem. Commun.* **2014**, *50*, 4396–4415. [[CrossRef](#)] [[PubMed](#)]
17. Shi, L.; Shao, D.; Wei, X.; Dunbar, K.R.; Wang, X. Enhanced Single-Chain Magnet Behavior via Anisotropic Exchange in a Cyano-Bridged  $\text{Mo}^{\text{III}}\text{-Mn}^{\text{II}}$  Chain. *Angew. Chem. Int. Ed.* **2020**, *59*, 10379–10384. [[CrossRef](#)]
18. Charytanowicz, T.; Jankowski, R.; Zychowicz, M.; Chorazy, S.; Sieklucka, B. The Rationalized Pathway from Field-Induced Slow Magnetic Relaxation in  $\text{Co}^{\text{II}}\text{-W}^{\text{IV}}$  Chains to Single-Chain Magnetism in Isotopological  $\text{Co}^{\text{II}}\text{-W}^{\text{V}}$  Analogues. *Inorg. Chem. Front.* **2022**, *9*, 1152–1170. [[CrossRef](#)]
19. Tan, P.; Yang, Y.; Lv, W.; Jing, R.; Cui, H.; Zheng, S.-J.; Chen, L.; Yuan, A.; Chen, X.-T.; Zhao, Y. A Cyanometallate- and Carbonate-Bridged Dysprosium Chain Complex with a Pentadentate Macrocyclic Ligand: Synthesis, Structure, and Magnetism. *N. J. Chem.* **2022**, *46*, 7892–7898. [[CrossRef](#)]
20. Miyasaka, H.; Madanbashi, T.; Saitoh, A.; Motokawa, N.; Ishikawa, R.; Yamashita, M.; Bahr, S.; Wernsdorfer, W.; Clérac, R. Cyano-Bridged  $\text{Mn}^{\text{III}}\text{-M}^{\text{III}}$  Single-Chain Magnets with  $\text{M}^{\text{III}} = \text{Co}^{\text{III}}, \text{Fe}^{\text{III}}, \text{Mn}^{\text{III}}, \text{and } \text{Cr}^{\text{III}}$ . *Chem. Eur. J.* **2012**, *18*, 3942–3954. [[CrossRef](#)]
21. Rams, M.; Peresypkina, E.V.; Mironov, V.S.; Wernsdorfer, W.; Vostrikova, K.E. Magnetic Relaxation of 1D Coordination Polymers  $\text{X}_2[\text{Mn}(\text{acacen})\text{Fe}(\text{CN})_6]$ ,  $\text{X} = \text{Ph}_4\text{P}^+, \text{Et}_4\text{N}^+$ . *Inorg. Chem.* **2014**, *53*, 10291–10300. [[CrossRef](#)]
22. Ferbinteanu, M.; Miyasaka, H.; Wernsdorfer, W.; Nakata, K.; Sugiura, K.; Yamashita, M.; Coulon, C.; Clérac, R. Single-Chain Magnet  $(\text{NEt}_4)[\text{Mn}_2(5\text{-MeOsalen})_2\text{Fe}(\text{CN})_6]$  Made of  $\text{Mn}^{\text{III}}\text{-Fe}^{\text{III}}\text{-Mn}^{\text{III}}$  Trinuclear Single-Molecule Magnet with an  $S = 9/2$  Spin Ground State. *J. Am. Chem. Soc.* **2005**, *127*, 3090–3099. [[CrossRef](#)]
23. Aguilà, D.; Jeannin, O.; Fourmigué, M.; Jeon, I.-R.  $\text{Mn}^{\text{III}}\text{-Fe}^{\text{III}}$  Heterometallic Compounds within Hydrogen-Bonded Supramolecular Networks Promoted by an  $[\text{Fe}(\text{CN})_5(\text{CNH})]^{2-}$  Building Block: Structural and Magnetic Properties. *Inorg. Chem.* **2018**, *57*, 7892–7903. [[CrossRef](#)] [[PubMed](#)]
24. Wei, X.-Q.; Qian, K.; Wei, H.-Y.; Wang, X.-Y. A One-Dimensional Magnet Based on  $[\text{Mo}^{\text{III}}(\text{CN})_7]^{4-}$ . *Inorg. Chem.* **2016**, *55*, 5107–5109. [[CrossRef](#)] [[PubMed](#)]
25. Wang, K.; Xia, B.; Wang, Q.-L.; Ma, Y.; Liao, D.-Z.; Tang, J. Slow Magnetic Relaxation Based on the Anisotropic Ising-Type Magnetic Coupling between the  $\text{Mo}^{\text{III}}$  and  $\text{Mn}^{\text{II}}$  Centers. *Dalton Trans.* **2017**, *46*, 1042–1046. [[CrossRef](#)] [[PubMed](#)]
26. Larionova, J.; Kahn, O.; Gohlen, S.; Ouahab, L.; Clérac, R. Structure, Ferromagnetic Ordering, Anisotropy, and Spin Reorientation for the Two-Dimensional Cyano-Bridged Bimetallic Compound  $\text{K}_2\text{Mn}_3(\text{H}_2\text{O})_6[\text{Mo}(\text{CN})_7]_2 \cdot 6\text{H}_2\text{O}$ . *J. Am. Chem. Soc.* **1999**, *121*, 3349–3356. [[CrossRef](#)]
27. Larionova, J.; Clérac, R.; Sanchiz, J.; Kahn, O.; Golhen, S.; Ouahab, L. Ferromagnetic Ordering, Anisotropy, and Spin Reorientation for the Cyano-Bridged Bimetallic Compound  $\text{Mn}_2(\text{H}_2\text{O})_5\text{Mo}(\text{CN})_7 \cdot 4\text{H}_2\text{O}$  ( $\alpha$  Phase). *J. Am. Chem. Soc.* **1998**, *120*, 13088–13095. [[CrossRef](#)]
28. Tomono, K.; Tsunobuchi, Y.; Nakabayashi, K.; Ohkoshi, S. Vanadium(II) Heptacyanomolybdate(III)-Based Magnet Exhibiting a High Curie Temperature of 110 K. *Inorg. Chem.* **2010**, *49*, 1298–1300. [[CrossRef](#)]
29. Gatteschi, D.; Sessoli, R.; Villain, J. *Molecular Nanomagnets*; Oxford University Press: Oxford, UK, 2006. [[CrossRef](#)]
30. Gao, S. *Molecular Nanomagnets and Related Phenomena*; Springer: New York, NY, USA, 2015; Volume 164.
31. Juan, B.; Fernando, L.; Fernández, J.F. (Eds.) *Molecular Magnets: Physics and Applications*. In *NanoScience and Technology*; Springer: Berlin/Heidelberg, Germany, 2014; pp. 1–395.
32. Dhers, S.; Feltham, H.L.C.; Brooker, S. A Toolbox of Building Blocks, Linkers and Crystallisation Methods Used to Generate Single-Chain Magnets. *Coord. Chem. Rev.* **2015**, *296*, 24–44. [[CrossRef](#)]
33. Glauber, R.J. Time-Dependent Statistics of the Ising Model. *J. Math. Phys.* **1963**, *4*, 294–307. [[CrossRef](#)]

34. Coulon, C.; Clérac, R.; Lecren, L.; Wernsdorfer, W.; Miyasaka, H. Glauber dynamics in a single-chain magnet: From theory to real systems. *Phys. Rev. B* **2004**, *69*, 132408. [[CrossRef](#)]
35. Zhang, W.X.; Breedlove, B.; Ishikawa, R.; Yamashita, M. Single-chain magnets: Beyond the Glauber model. *RSC Adv.* **2013**, *3*, 3772–3798. [[CrossRef](#)]
36. Chibotaru, L.F.; Hendrickx, M.F.A.; Clima, S.; Larionova, J.; Ceulemans, A.J. Magnetic Anisotropy of [Mo(CN)<sub>7</sub>]<sup>4-</sup> Anions and Fragments of Cyano-Bridged Magnetic Networks. *Phys. Chem. A* **2005**, *109*, 7251–7257. [[CrossRef](#)] [[PubMed](#)]
37. Manoli, J.M.; Potvin, C.; Bregeault, J.M.J. Crystal structure of potassium heptacyanorhenate(III) dehydrate. *Chem. Soc. Dalton Trans.* **1980**, *1*, 192–195. [[CrossRef](#)]
38. Bennett, M.V.; Long, J.R. New Cyanometalate Building Units: Synthesis and Characterization of [Re(CN)<sub>7</sub>]<sup>3-</sup> and [Re(CN)<sub>8</sub>]<sup>3-</sup>. *J. Am. Chem. Soc.* **2003**, *125*, 2394–2395. [[CrossRef](#)]
39. Mironov, V.S. Origin of Dissimilar Single-Molecule Magnet Behavior of Three Mn<sup>II</sup><sub>2</sub>Mo<sup>III</sup> Complexes Based on [Mo<sup>III</sup>(CN)<sub>7</sub>]<sup>4-</sup> Heptacyanomolybdate: Interplay of Mo<sup>III</sup>–CN–Mn<sup>II</sup> Anisotropic Exchange Interactions. *Inorg. Chem.* **2015**, *54*, 11339–11355. [[CrossRef](#)] [[PubMed](#)]
40. Rossman, G.R.; Tsay, F.D.; Gray, H.B. Spectroscopic and magnetic properties of heptacyanomolybdate(III). Evidence for pentagonal-bipyramidal and monocapped trigonal-prismatic structures. *Inorg. Chem.* **1973**, *12*, 824–829. [[CrossRef](#)]
41. Peresyphkina, E.V.; Samsonenko, D.G.; Vostrikova, K.E. Heterobimetallic coordination polymers involving 3d metal complexes and heavier transition metals cyanometallates. *J. Solid State Chem.* **2015**, *224*, 107–114. [[CrossRef](#)]
42. Bonadies, J.A.; Kirk, M.L.; Lah, M.S.; Kessissoglou, D.P.; Hatfield, W.E.; Pecoraro, V.L. Structurally diverse manganese(III) Schiff base complexes: Chains, dimers, and cages. *Inorg. Chem.* **1989**, *28*, 2037–2044. [[CrossRef](#)]
43. Peresyphkina, E.V.; Vostrikova, K.E. 2[Mn(acacen)]<sup>+</sup> + [Fe(CN)<sub>5</sub>NO]<sup>2-</sup> Polynuclear Heterobimetallic Coordination Compounds of Different Dimensionality in the Solid State. *Dalton Trans.* **2012**, *41*, 4100. [[CrossRef](#)]
44. Samsonenko, D.G.; Paulsen, C.; Lhotel, E.; Mironov, V.S.; Vostrikova, K.E. [Mn<sup>III</sup>(SchiffBase)]<sub>3</sub>[Re<sup>IV</sup>(CN)<sub>7</sub>], Highly Anisotropic 3D Coordination Framework: Synthesis, Crystal Structure, Magnetic Investigations, and Theoretical Analysis. *Inorg. Chem.* **2014**, *53*, 10217–10231. [[CrossRef](#)]
45. Wu, D.-Q.; Shao, D.; Wei, X.-Q.; Shen, F.-X.; Shi, L.; Kempe, D.; Zhang, Y.-Z.; Dunbar, K.R.; Wang, X.-Y. Reversible On-Off Switching of a Single-Molecule Magnet via a Crystal-to-Crystal Chemical Transformation. *J. Am. Chem. Soc.* **2017**, *139*, 11714–11717. [[CrossRef](#)]
46. Sukhikh, T.; Wernsdorfer, W.; Vostrikova, K. Slow Magnetic Relaxation in Neutral 0D and 1D Assemblies of a Mn(III) Schiff Base Complex and Heptacyanorhenate(IV). *Magnetochemistry* **2022**, *8*, 126. [[CrossRef](#)]
47. Ishikawa, R.; Nakano, M.; Breedlove, B.K.; Yamashita, M. Syntheses, Structures, and Magnetic Properties of Discrete Cyano-Bridged Heterodinuclear Complexes Composed of Mn<sup>III</sup>(Salen)-Type Complex and M<sup>III</sup>(CN)<sub>6</sub> Anion (M<sup>III</sup> = Fe, Mn, and Cr). *Polyhedron* **2013**, *64*, 346–351. [[CrossRef](#)]
48. Vostrikova, K.E. Homoleptic Osmium Cyanide Complexes: Synthesis and Perspective Application in Molecular Magnetism. In *Osmium: Synthesis Characterization and Applications*; Wise, G., Ed.; Nova Science Publishers: New York, NY, USA, 2015; pp. 43–78, ISBN 978-1-63483-517-6.
49. Lescouëzec, R.; Toma, L.M.; Vaissermann, J.; Verdaguer, M.; Delgado, F.S.; Ruiz-Pérez, C.; Lloret, F.; Julve, M. Design of Single Chain Magnets through Cyanide-Bearing Six-Coordinate Complexes. *Coord. Chem. Rev.* **2005**, *249*, 2691–2729. [[CrossRef](#)]
50. Sakamoto, F.; Sumiya, T.; Fujita, M.; Tada, T.; Tan, X.S.; Suzuki, E.; Okura, I.; Fujii, Y. T-Site Selective Photocleavage of DNA by Cationic Schiff Base Complex of Manganese(III). *Chem. Lett.* **1998**, *27*, 1127–1128. [[CrossRef](#)]
51. Pinkowicz, D.; Podgajny, R.; Nowicka, B.; Chorazy, S.; Reczyński, M.; Sieklucka, B. Magnetic Clusters Based on Octacyanidometallates. *Inorg. Chem. Front.* **2015**, *2*, 10–27. [[CrossRef](#)]
52. Harris, T.D.; Bennett, M.V.; Clérac, R.; Long, J.R. [ReCl<sub>4</sub>(CN)<sub>2</sub>]<sup>2-</sup>: A High Magnetic Anisotropy Building Unit Giving Rise to the Single-Chain Magnets (DMF)<sub>4</sub>MReCl<sub>4</sub>(CN)<sub>2</sub> (M = Mn, Fe, Co, Ni). *J. Am. Chem. Soc.* **2010**, *132*, 3980–3988. [[CrossRef](#)]
53. Miyasaka, H.; Ieda, H.; Re, N.; Crescenzi, R.; Floriani, C. Assembling Bi-, Tri- and Pentanuclear Complexes into Extended Structures Using a Desolvation Reaction: Synthesis, Structure, and Magnetic Properties of Manganese(III)–Schiff-Base–Hexacyanoferrate Polymeric Compounds and Their Derived Extended Structures. *Inorg. Chem.* **1998**, *37*, 255–263. [[CrossRef](#)]
54. Nakamura, K.; Sasada, T. Statistical Mechanics of Classical One-Dimensional Heisenberg Ferromagnets with Single-Site Anisotropy. *J. Phys. C Solid State Phys.* **1978**, *11*, 331–343. [[CrossRef](#)]
55. Miyasaka, H.; Julve, M.; Yamashita, M.; Clérac, R. Slow Dynamics of the Magnetization in One-Dimensional Coordination Polymers: Single-Chain Magnets. *Inorg. Chem.* **2009**, *48*, 3420–3437. [[CrossRef](#)]
56. Moreno Pineda, E.; Wernsdorfer, W.; Vostrikova, K.E. Very Anisotropic 2D Molecular Magnetic Materials Based on Pentagonal Bipyramidal Heptacyanidorhenate(IV). *Materials* **2022**, *15*, 8324. [[CrossRef](#)]
57. Miyasaka, H.; Okawa, H.; Miyazaki, A.; Enoki, T. Synthesis, Crystal and Network Structures, and Magnetic Properties of a Hybrid Layered Compound: [K(18-Cr)(2-PrOH)<sub>2</sub>][{Mn(Acacen)}<sub>2</sub>{Fe(CN)<sub>6</sub>}] (18-Cr = 18-Crown-6-Ether, Acacen = N,N'-Ethylenebis(Acetylacetyloneimine)). *Inorg. Chem.* **1998**, *37*, 4878–4883. [[CrossRef](#)] [[PubMed](#)]
58. Kou, H.-Z.; Ni, Z.-H.; Zhou, B.C.; Wang, R.-J. A Cyano-Bridged Molecule-Based Magnet Containing Manganese(III) Schiff Base and Octacyanotungstate(V) Building Blocks. *Inorg. Chem. Commun.* **2004**, *7*, 1150–1153. [[CrossRef](#)]
59. Sukhikh, T.; Vostrikova, K. Assembly of Mn(III) Schiff Base Complexes with Heptacyanorhenate(IV). *Inorganics* **2017**, *5*, 59. [[CrossRef](#)]

60. Zhang, C.-G.; Tian, G.-H.; Ma, Z.-F.; Yan, D.-Y. Synthesis, crystal structure and properties of a novel di- $\mu_2$ -aqua bridged binuclear manganese(III) Schiff base complex  $[\text{Mn}(\text{vanen})(\text{H}_2\text{O})_2]_2(\text{ClO}_4)_2 \cdot 2\text{H}_2\text{O}$ . *Trans. Met. Chem.* **2000**, *25*, 270–273. [[CrossRef](#)]
61. Manakin, Y.V.; Mironov, V.S.; Bazhenova, T.A.; Lyssenko, K.A.; Gilmutdinov, I.F.; Bikbaev, K.S.; Masitov, A.A.; Yagubskii, E.B.  $(\text{Et}_4\text{N})[\text{Mo}^{\text{III}}(\text{DAPBH})\text{Cl}_2]$ , the first pentagonal-bipyramidal Mo(III) complex with a  $\text{N}_3\text{O}_2$ -type Schiff-base ligand: Manifestation of unquenched orbital momentum and Ising-type magnetic anisotropy. *Chem. Commun.* **2018**, *54*, 10084–10087. [[CrossRef](#)]